Title page

Two distinct phases of chloroplast biogenesis during de-etiolation in *Arabidopsis thaliana*

Authors: Rosa Pipitone[1], Simona Eicke[2], Barbara Pfister[2], Gaetan Glauser[3], Denis Falconet[4], Clarisse Uwizeye[4], Thibaut Pralon[1], Samuel Zeeman[2], Felix Kessler[1,*], Emilie Demarsy[1,5,*]

Authors affiliations:
[1] Plant Physiology Laboratory, University of Neuchâtel, Neuchâtel, Switzerland
[2] Institute of Molecular Plant Biology, Department of Biology ETH Zurich, Zurich, Switzerland
[3] Neuchâtel Platform of Analytical Chemistry, University of Neuchâtel, Neuchâtel, Switzerland
[4] Univ. Grenoble Alpes, CNRS, CEA, INRAE, IRIG-DBSCI-LPCV, 38000 Grenoble, France
[5] Department of Botany and Plant Biology, University of Geneva, CH-1211 Geneva 4, Switzerland

*Corresponding authors:

Emilie Demarsy, emilie.demarsy@unige.ch

Felix Kessler, felix.kessler@unine.ch

Running title (max 50 characters):

Dynamics of chloroplast biogenesis

Impact statement: Serial Block Face Scanning Electron Microscopy (SBF-SEM) associated with biomolecular analysis show that chloroplast differentiation proceeds by distinct 'Structure Establishment' and 'Chloroplast Proliferation' phases, each with differential protein and lipid regulation.

Keywords

Thylakoid / Chloroplast / Photosynthesis / SBF-SEM / Proteomics / Arabidopsis

Abstract

Light triggers chloroplast differentiation whereby the etioplast transforms into a photosynthesizing chloroplast and the thylakoid rapidly emerges. However, the sequence of events during chloroplast differentiation remains poorly understood. Using Serial Block Face Scanning Electron Microscopy (SBF-SEM), we generated a series of chloroplast 3D reconstructions during differentiation, revealing chloroplast number and volume and the extent of envelope and thylakoid membrane surfaces. Furthermore, we used quantitative lipid and whole proteome data to complement the (ultra)structural data, providing a time-resolved, multi-dimensional description of chloroplast differentiation. This showed two distinct phases of chloroplast biogenesis: an initial photosynthesis-enabling 'Structure Establishment Phase' followed by a 'Chloroplast Proliferation Phase' during cell expansion. Moreover, these data detail thylakoid membrane expansion during de-etiolation at the seedling level and the relative contribution and differential regulation of proteins and lipids at each developmental stage. Altogether, we establish a roadmap for chloroplast differentiation, a critical process for plant photoautotrophic growth and survival.

Introduction

Seedling development relies on successful chloroplast biogenesis, ensuring the transition from heterotrophic to autotrophic growth. Light is a crucial factor for chloroplast differentiation. For seeds that germinate in the light, chloroplasts may differentiate directly from proplastids present in cotyledons. However, as seeds most often germinate underneath soil, seedling development typically begins in darkness and follows a skotomorphogenic program called etiolation, characterized by rapid hypocotyl elongation and etioplast development. Light promotes seedling de-etiolation, which involves a series of morphological changes, such as cotyledon expansion, hypocotyl growth inhibition, and greening, that accompanies the onset of photosynthesis in chloroplasts. During de-etiolation, etioplast–chloroplast transition is thereby rapidly triggered by light following seedling emergence at the soil surface (Solymosi and Schoefs, 2010; Weier and Brown, 1970). A hallmark of chloroplast differentiation is the biogenesis of thylakoids, a network of internal membranes where the components of the photosynthetic electron transport chain assemble. Thylakoid biogenesis and the onset of photosynthesis rely on the concerted synthesis and coordinated assembly of lipids and proteins in both space and time.

The thylakoids harbor the photosynthetic electron transport chain, which is composed of three complexes: photosystem II (PSII), the cytochrome b_6f complex (Cyt b_6f), and photosystem I (PSI). Electron transfer between these complexes is facilitated by mobile electron carriers, specifically the low-molecular-weight, membrane-soluble plastoquinone (electron transfer from PSII to Cyt b_6f) and the lumenal protein plastocyanin (electron transfer from Cyt b_6f to PSI). Electron transfer leads to successive reduction and oxidation of electron transport chain components. The final reduction step catalyzed by ferredoxin-NADP(+) reductase (FNR) leads to NADPH production. Oxidation of water by PSII and of plastoquinone by Cyt b_6f releases protons into the lumen, generating a proton gradient across the thylakoid membrane that drives the activity of the thylakoid-localized chloroplast ATP synthase complex. Each of the photosynthetic complexes consists of multiple subunits encoded by the plastid or nuclear genome. PSII and PSI have core complexes comprising 25–30 and 15 proteins, respectively (Amunts and Nelson, 2009; Caffarri et al., 2014). The antenna proteins from the Light Harvesting Complexes (LHC) surround the PSI and PSII core complexes contributing to the formation of supercomplexes. Cyt b_6f is an eight-subunit dimeric complex. Each complex of the electron transport chain has a specific dimension, orientation, and location within the thylakoid membrane, occupying a defined surface, and their dimensions have been reported in several studies giving congruent results (Caffarri et al., 2014; Kurisu et al., 2003; Van

97 Bezouwen et al., 2017). During de-etiolation, massive protein synthesis is required for
98 assembly of the highly abundant photosynthetic complexes embedded in thylakoids.
99 Chloroplast proteins encoded by the nuclear genome must be imported from the cytoplasm.
100 The general chloroplast protein import machinery is composed of the multimeric complexes
101 Translocon of Outer membrane Complex (TOC) and Translocon of Inner membrane Complex
102 (TIC), and selective import is based on specific recognition of transit peptide sequences and
103 TOC receptors (Agne and Kessler, 2010; Richardson and Schnell, 2019).
104
105 Reminiscent of their cyanobacterial origin, chloroplast membranes are composed mostly of
106 glycolipids (mono- and di-galactosyldiacylglycerol; MGDG and DGDG) and are poor in
107 phospholipids compared to other membranes in the cell (Bastien et al., 2016; Block et al.,
108 1983; Kobayashi, 2016). Galactolipids comprise a glycerol backbone esterified to contain a
109 single (MGDG) or double (DGDG) galactose units at the *sn*1 position and two fatty acid chains
110 at the *sn*2 and *sn*3 positions. In addition to the number of galactose units at *sn*1, galactolipids
111 also differ by the length and degrees of saturation of the fatty acid chains. In some species,
112 including Arabidopsis, galactolipid synthesis relies on two different pathways, defined as the
113 eukaryotic and prokaryotic pathway depending on the organellar origin of the diacylglycerol
114 precursor. The eukaryotic pathway requires the import of diacyl-glycerol (DAG) synthesized in
115 the endoplasmic reticulum (ER) into the plastids and is referred to as the ER pathway, whereas
116 the prokaryotic pathway is entirely restricted to the plastid (PL) and is referred to as the PL
117 pathway (Ohlrogge and Browse, 1995). As signatures, ER pathway–derived galactolipids
118 harbor an 18-carbon chain whereas PL pathway–derived galactolipids harbor a 16-carbon
119 chain at the *sn*2 position. In addition to constituting the lipid bilayer, galactolipids are integral
120 components of photosystems and thereby contribute to photochemistry and photoprotection
121 (Aronsson et al., 2008; Kobayashi, 2016). Thylakoids also contain neutral lipids such as
122 chlorophyll, carotenoids, tocopherols, and plastoquinone. These may exist freely or be
123 associated with the photosynthetic complexes, having either a direct role in photosynthesis
124 (chlorophyll, carotenoids, plastoquinone) or participating indirectly in the optimization of light
125 usage and/or mitigation of potentially damaging effects (tocopherols in addition to carotenoids
126 and plastoquinone) (Hashimoto et al., 2003; Van Wijk and Kessler, 2017).
127
128 Past studies used conventional electron microscopy to first describe the architecture of the
129 thylakoid membrane network. Based on these 2D observations, researchers proposed that
130 plant thylakoid membranes are organised as single lamellae connected to appressed multi-
131 lamellar regions called grana. How these lamellae are interconnected was revealed only later
132 following the development of 3D electron microscopic techniques. Tremendous technological
133 progress in the field of electron microscopy has been made recently, leading to improved

descriptions of chloroplast ultrastructure (Daum et al., 2010; Daum and Kühlbrandt, 2011). Electron tomography substantially improved our comprehension of the 3D organisation of the thylakoid network in chloroplasts at different developmental stages and in different photosynthetic organisms, including Arabidopsis (Austin and Staehelin, 2011; Liang et al., 2018), Chlamydomonas (Engel et al., 2015), runner bean (Kowalewska et al., 2016), and *Phaeodactylum tricornutum* (Flori et al., 2017). Electron tomography also provided quantitative information on thylakoid structure such as the thylakoid layer number within the grana stack and the thickness of the stacking repeat distance of grana membrane (Daum et al., 2010; Kirchhoff et al., 2011). These quantitative data allowed a greater understanding of the spatial organisation of the thylakoid membrane in relation to the embedded photosynthetic complexes (Wietrzynski et al., 2020). Although electron tomography offers extraordinary resolution at the nanometer level, its main drawback is a limit to the volume of the observation, enabling only a partial 3D reconstruction of a chloroplast. SBF-SEM technology allows a much larger volume to be studied and reconstructed in 3D to show cellular organisation (Peddie and Collinson, 2014; Pinali and Kitmitto, 2014).

In combination with electron microscopy, biochemical fractionation of thylakoids has revealed differential lipid and protein compositions of the grana and the stroma lamellae. The grana are enriched in DGDG and PSII whereas the stroma lamellae are enriched in MGDG, Cyt *b6/f*, and PSI (Demé et al., 2014; Koochak et al., 2019; Tomizioli et al., 2014; Wietrzynski et al., 2020). Changes in lipid and protein compositions during etioplast–chloroplast transition are tightly linked to the thylakoid architecture. In particular, changes in MGDG to DGDG ratio are correlated with the transition from prolamellar body (PLB) and prothylakoid (PT) structures (tubular membrane) to thylakoid membranes (lamellar structure) (Bottier et al., 2007; Demé et al., 2014; Mazur et al., 2019).

Individual studies have provided much insight regarding specific dynamics of the soluble chloroplast proteome, the chloroplast transcriptome, photosynthesis-related protein accumulation and photosynthetic activity, chloroplast lipids, and changes in thylakoid architecture (Armarego-Marriott et al., 2019; Dubreuil et al., 2018; Kleffmann et al., 2007; Kowalewska et al., 2016; Liang et al., 2018; Rudowska et al., 2012). However, these studies were mostly qualitative, focused on one or two aspects, and were performed in different model organisms. Therefore, chemical data related to thylakoid biogenesis remain sparse and quantitative information is rare. Here, we present a systems-level study that integrates quantitative information on ultrastructural changes of the thylakoids with lipid and protein composition during de-etiolation of Arabidopsis seedlings.

175 ## Results

176 ### The photosynthetic machinery is functional after 14 h of de-etiolation

177

178 We analysed etioplast–chloroplast transition in Arabidopsis seedlings grown in the absence of
179 exogenous sucrose for 3 days in darkness and then exposed to constant white light (Figure
180 1A). These experimental conditions were chosen to avoid effects of exogenous sucrose on
181 seedling development and variations due to circadian rhythm. Upon illumination, the etiolated
182 seedlings switched from the skotomorphogenic to the photomorphogenic developmental
183 program, evidenced by opening of the apical hook and cotyledon greening and expansion
184 (Figure 1B). We stopped the analysis following 96 h of illumination (T96), before the
185 emergence of the primary leaves. Samples were collected at different selected time points
186 during de-etiolation(Figure 1A).
187 In angiosperms, chlorophyll synthesis arrests in the dark but starts immediately upon seedling
188 irradiation (Von Wettstein et al., 1995). Chlorophyll levels in whole seedlings increased within
189 the first 4 h of illumination (T4) and continued to increase linearly during subsequent
190 illumination as the seedlings grew (Figure 1C). To evaluate photosynthetic efficiency during
191 de-etiolation, we measured chlorophyll fluorescence and calculated the maximum quantum
192 yield of PSII (Fv/Fm, Figure 1D and Figure 1- figure supplement 1). PSII maximum quantum
193 yield increased during the initial period of illumination and was near the maximal value of 0.8
194 at 14 h of light exposure (T14), independent of light intensity (Figure 1D and Figure 1- figure
195 supplement 1A). Other photosynthetic parameters (photochemical quenching, qP and PSII
196 quantum yield in the light, ΦPSII, Figure 1-figure supplement 1 B and C) reached maximum
197 values at T14 and remained stable thereafter, indicating that the assembly of fully functional
198 photosynthetic machinery occurs within the first 14 h of de-etiolation, and that further
199 biosynthesis of photosynthesis related compounds is efficiently coordinated.

200

201 ### Major thylakoid structural changes occur within 24 h of de-etiolation

202

203 We determined the dynamics of thylakoid biogenesis during the etioplast–chloroplast transition
204 by observing chloroplast ultrastructure in cotyledons using transmission electron microscopy
205 (TEM) (Figure 2). Plastids present in cotyledons of etiolated seedlings displayed the typical
206 etioplast ultrastructure with a paracrystalline PLB and tubular PTs (Figure 2A). The observed
207 PLBs were constituted of hexagonal units with diameters of 0.8–1 µm (Figure 2E). By T4, the
208 highly structured PLBs progressively disappeared and thylakoid lamellae were formed (Figure
209 2B). The lamellae were blurry and their thickness varied between 15 and 70 nm (Figure 2F).
210 After 24 h of illumination (T24), the density of lamellae per chloroplast was higher than that at

211 T4 due to an increase in lamellar length and number. Appressed regions corresponding to
212 developing grana stacks also appeared by T24 (Figure 2C and G). These early grana stacks
213 consisted of 2–6 lamellae with a thickness of 13 nm each (Figure 2- figure supplement 1). In
214 addition, starch granules were present at T24, supporting the notion that these chloroplasts
215 are photosynthetically functional and able to assimilate carbon dioxide (CO_2). At T96, thylakoid
216 membrane organisation was visually similar to that at T24, but with more layers per grana (up
217 to 10 lamellae per grana; Figures 3D and H). In addition, singular lamella thickness at T96
218 increased by 2–3 nm compared to that at T24 (Figure 2- figure supplement 1). The major
219 differences observed between T24 and T96 were increases in starch granule size and number
220 and overall chloroplast size. Etioplast average length (estimated by measuring the maximum
221 distance on individual slices) was 2 µm (± 0.9, n=10) in the dark (T0), whereas chloroplast
222 average length was 6 µm (± 1.62, n=10) at T96 (Table1). Collectively, these data show that
223 photosynthetically functional thylakoid membranes form rapidly during the first 24 h of de-
224 etiolation. This implies that there are efficient mechanisms for thylakoid assembly and
225 structural organisation. Subsequent changes seem to involve the expansion of pre-existing
226 structures (i.e. lamellae length and grana size) and the initiation of photosynthetic carbon
227 fixation (reflected by starch content).
228
229
230

231 ## Quantitative analysis of thylakoid surface area per chloroplast during de-etiolation

232
233 To visualize entire chloroplasts and thylakoid networks in 3D, and to obtain a quantitative view
234 of the total thylakoid surface area during chloroplast development, we prepared and imaged
235 cotyledons at different developmental stages by SBF-SEM (Figure 3 A-D). PLBs, thylakoids,
236 and envelope membranes were selected, and segmented images were used for 3D
237 reconstruction (Figure 3E–N, and videos 1–4; see also Figure 2- figure supplement 1 and
238 Figure 4- figure supplement 1 for grana segmentation). Similar to that observed by TEM
239 (Figure 2), a drastic switch from PLB to thylakoid membrane occurred by T4: the typical
240 structure of the PLB connected to PTs disappeared leaving only elongated lamellar structures
241 (Figure 3E–F and videos 1 and 2). At T24 and T96, thylakoid membranes were organised in
242 appressed and non-appressed regions and large spaces occupied by starch granules were
243 observed (Figure 3G–H and videos 3 and 4). 3D reconstruction revealed a change in plastid
244 shape from ovoid at T0 and T4 to hemispheric at T24 and T96 (Figure 3I–N).
245

246 Using 3D reconstruction of the thylakoid network for 3 or 4 chloroplasts for each developmental
247 stage, quantitative data such as chloroplast volume and membrane surface area were
248 extracted and calculated (Figure 4A and B, Figure 4 figure supplement 1 and Table 1). The
249 total chloroplast volume increased about 11-fold from T4 (9.4 μm^3) to T96 (112.14 μm^3) (Table
250 1). In parallel, the thylakoid surface area increased about 30-fold reaching 2,086 (± 393) μm^2
251 per chloroplast at T96 (Figure 4A and Table 1). The surface area increased drastically between
252 T4 and T24 (about 22-fold) and much less (about 1.4-fold) between T24 and T96. Accordingly,
253 quantification of the envelope surface area indicated that the ratio of the thylakoid to envelope
254 surface area increased drastically from T4 to T24, but decreased slightly between T24 and
255 T96 (Table 1).
256 Our observations indicated that chloroplast development during the first 96 hours of de-
257 etiolation could be separated into two phases: a first phase reflected by qualitative changes
258 (i.e. structure establishment and reorganisation of the thylakoid network architecture) and a
259 second phase (starting before T24) during which thylakoid surface increased due to the
260 expansion and stacking of lamellae. We further analysed these temporal processes at the
261 molecular level focusing on proteins and lipids that constitute the thylakoid membrane.
262
263

264 Dynamics of plastid proteins related to thylakoid biogenesis

265
266 We analysed the full proteome to reveal the dynamics of protein accumulation during de-
267 etiolation. Total proteins were prepared from 3-day-old etiolated seedlings exposed to light for
268 0–96 h (eight time points; Figure 1A) and quantified by label-free shot-gun mass spectrometry.
269 For relative quantification of protein abundances between different samples, peptide ion
270 abundances were normalized to total protein (see Materials and Methods). We considered
271 further only those proteins that were identified with a minimum of two different peptides (with
272 at least one being unique; see Methods for information on protein grouping), resulting in the
273 robust identification and quantification of more than 5,000 proteins. Fold changes of protein
274 abundances between two time points were regarded as significant if their adjusted *p*-value (i.e.
275 the *q*-value) was < 0.01.
276 The first 12 h of illumination (T12) saw very few significant changes in protein abundance
277 (Supplemental Dataset 1). After 8 h of illumination (T8), we observed decreased abundance
278 of only one protein (the photoreceptor cryptochrome 2, consistent with its photolabile property)
279 and increased levels of only three proteins, which belonged to the chlorophyll a/b binding
280 proteins category involved in photoprotection (AT1G44575 = PsbS; AT4G10340= Lhcb5;
281 AT1G15820= Lhcb6; (Chen et al., 2018; Li et al., 2000). A drastic change of proteome
282 composition occurred by T24, with 467 proteins showing a significant increase in abundance

283 with over 2-fold change (FC>2) compared with the etiolated stage, and 150 proteins showing
284 a significant decrease with over 2-fold change (FC<0.5). As expected, the 100 most-
285 upregulated proteins comprised proteins related to photosynthesis, proteins constituting the
286 core and antennae of photosystems, and proteins involved in carbon fixation (Supplemental
287 Dataset 1).
288 To monitor the dynamics of the plastidial proteome, we selected proteins predicted to localize
289 to the plastid (consensus localization from SUBA4; Hooper et al., 2017). Generation of a global
290 heatmap for each of the 1,112 potential plastidial proteins revealed different accumulation
291 patterns (Supplemental Dataset 2 and Figure 5- figure supplement 1). Hierarchical clustering
292 showed a categorization into six main clusters. Cluster 1 (purple) contained proteins whose
293 relative amounts decreased during de-etiolation. Clusters 2, 5, and 6 (pink, light green, and
294 dark green, respectively) contained proteins whose relative amounts increased during de-
295 etiolation but differed with respect to the amplitude of variations. Proteins in clusters 2 and 6
296 displayed the largest amplitude of differential accumulation. Gene ontology (GO) analysis (Mi
297 et al., 2019) indicated a statistically significant overrepresentation of proteins related to the
298 light reactions of photosynthesis in clusters 2 and 6 (Supplemental Dataset 2).
299 Underrepresentation of organic acid metabolism, in particular carboxylic acid metabolism,
300 characterized cluster 2, whereas overrepresentation of carboxylic acid biosynthesis and
301 underrepresentation of photosynthetic light reactions were clear features of cluster 3. Protein
302 levels in cluster 3 changed only moderately during de-etiolation in contrast with proteins levels
303 in cluster 2. No biological processes were significantly over- or underrepresented in clusters
304 1, 4, and 5.
305 To analyse the dynamics of proteins related to thylakoid biogenesis, we selected specific
306 proteins and represented their pattern of accumulation during de-etiolation (Figure 5). We
307 included proteins constituting protein complexes located in thylakoids (complexes constituting
308 the electron transport chain and the ATP synthase complex) and proteins involved in
309 chloroplast lipid metabolism, chlorophyll synthesis, and protein import into the chloroplast. In
310 agreement with that depicted in the global heatmap (Figure 5- figure supplement 1), all
311 photosynthesis-related proteins increased in abundance during de-etiolation (Figure 5A).
312 However, our hierarchical clustering did not show any particular clustering per complex . Only
313 few chloroplast-localized proteins related to lipid biosynthesis were present in our proteomics
314 data set. Among the eight detected proteins, two appeared differentially regulated; fatty acid
315 binding protein 1 (FAB1) and fatty acid desaturase 7 (FAD7) levels increased only between 72
316 h of illumination (T72) and T96, whereas the other proteins gradually accumulated over the
317 course of de-etiolation (Figure 5B). Etioplasts initiate synthesis of chlorophyll precursors that
318 are blocked at the level of protochlorophyllide synthesis, with protochlorophyllide
319 oxidoreductase A (PORA) in its inactive form accumulating to high levels in the etioplast before

320 subsequently decreasing at the protein level upon activation and degradation following light
321 exposure (Blomqvist et al., 2008; Runge et al., 1996; Von Wettstein et al., 1995). In agreement,
322 illumination resulted in increased amounts of all detected proteins of the chlorophyll
323 biosynthesis pathway, except PORA, which clearly decreased and was separated from other
324 chlorophyll-related proteins (Figure 5C). We also selected proteins involved in protein import
325 in chloroplasts, focusing on the TOC-TIC machinery (Figure 5D) that is the major route for
326 plastid protein import and essential for chloroplast biogenesis (Kessler and Schnell, 2006).
327 Past studies identified several TOC preprotein receptors that are proposed to display
328 differential specificities for preprotein classes (Bauer et al., 2000; Bischof et al., 2011). The
329 composition of plastid import complexes varies with developmental stages and in different
330 tissues, thereby adjusting the selectivity of the import apparatus to the demands of the plastid
331 and influencing its proteome composition (Demarsy et al., 2014; Kubis et al., 2003).
332 Accordingly, the TOC receptors TOC120 and TOC132, which are important for the import of
333 proteins in non-photosynthetic tissues, were more abundant in etioplasts compared to fully-
334 developed chloroplasts (compare T0 and T96). TOC120 and TOC132 were part of a cluster
335 separated from other components of the plastid machinery, such as the TOC159 receptor
336 associated with large-scale import of proteins in chloroplasts. The general import channel
337 TOC75 (TOC75 III) maintained stable expression levels throughout de-etiolation, reflecting its
338 general role in protein import. All other components clustered with TOC159 and displayed
339 gradual increases in accumulation during de-etiolation. Most of these components have not
340 been reported to confer selectivity to the import machinery, which suggests an overall increase
341 of chloroplast protein import capacity.
342
343
344 To validate and complement our proteomic data, we used immunoblot analysis to detect and
345 quantify representative proteins of the photosynthetic complexes. Overall, immunoblot and
346 proteomics provided similar results (Figure 6 and Figure 6- figure supplement 1). PsbA and
347 PsbD (PSII reaction center core), PsbO (Oxygen Evolving Complex), and Lhcb2 (outer
348 antenna complex) proteins were detectable in seedlings at T0, gradually increasing thereafter.
349 Accumulation of the PSI proteins PsaC and PsaD and the Cyt b_6f complex protein PetC started
350 later; these proteins were detectable starting at T8 (Figure 6A and Figure 6- figure supplement
351 1). Interestingly, AtpC (ATP synthase complex) was detectable in the etioplast, as described
352 previously (Plöscher et al., 2011). Other proteins were selected as markers of etioplast–
353 chloroplast transition. As expected, ELIPs (Early Light Induced Protein) transiently
354 accumulated upon the dark-to-light transition (Figure 6A) (Kimura et al., 2003). As in the
355 proteome analysis, PORA accumulated in etiolated seedlings (T0) and then progressively
356 disappeared upon light exposure. We performed absolute quantification for PsbA, PsaC, and

357 PetC proteins using recombinant proteins as standards (Figure 6B and C and Figure 6- figure
358 supplement 1). Quantitative data (nmol/seedling) were obtained and normalized using the last
359 time point (Figure 6C) to compare the dynamics of protein accumulation. In addition, the
360 comparison of PsbA and PsaC (representative proteins of PSII and PSI, respectively) showed
361 that PsbA levels were about twice that of PsaC at T96 (Figure 6B and C).
362
363
364 ## Dynamics of chloroplast membrane lipids
365
366 Total lipids were extracted from seedlings collected at different time points during de-etiolation
367 (T0, T4, T8, T12, T24, T48, T72, and T96), analysed by ultra-high pressure liquid
368 chromatography–mass spectrometry (UHPLC-MS), and quantified against pure standards
369 (supplemental Dataset 3). We analysed the quantity and kinetics of accumulation of 12
370 different species of galactolipids (Figure 7A and B). MGDG 18:3/16:3, MGDG 18:3/18:3,
371 MGDG 18:3/16:1, DGDG 18:3/18:3, and DGDG 18:3/16:0 were the most abundant lipids
372 detected at all time points. Accumulation of all galactolipids increased upon de-etiolation;
373 however, clustering analysis identified two distinct kinetic patterns. One group displayed a leap
374 between T8 and T12, whereas the other group showed a more gradual increase during the de-
375 etiolation period (Figure 7C). Interestingly, the two clusters separated the lipids according to
376 the two pathways described for galactolipid synthesis, namely the ER and PL pathways (Figure
377 7A and B) (Marechal et al., 1997; Ohlrogge and Browse, 1995). During early stages of de-
378 etiolation (T0–T24), we observed an incremental accumulation of MGDG and DGDG
379 galactolipids derived from the ER pathway, whereas galactolipids from the PL pathway started
380 to accumulate at T24 (Figure 7A and B). The MGDG/DGDG ratio decreased between T0 and
381 T8. This was associated with the transition from PLB (cubic lipid phase) to thylakoid membrane
382 (lamellar structure) (Bottier et al., 2007). The MGDG/DGDG ratio started to increase gradually
383 at T8 and was constant by T72 and T96 (Figure 7D).
384
385
386
387 ## Identification of a chloroplast division phase
388
389 We observed a massive increase in the accumulation of photosynthesis-related proteins and
390 galactolipids between T24 and T96, corresponding to FC>2 in the levels of all major chloroplast
391 proteins and lipids (Figures 6 and 7). Intriguingly, the total thylakoid surface per chloroplast
392 increased by only 41 % between these two time points (Figure 4A and Table 1). We reasoned
393 that the increase in chloroplast proteins and lipids between T24 and T96 could be explained

394 by increased chloroplast number (per cell and thus per seedling) and thus total thylakoid
395 surface per seedling. We therefore determined chloroplast number per cell and the cell number
396 and volume for each developmental stage through SBF-SEM analysis (T0, T4, T24, and T96)
397 and confocal microscopy analysis for intermediary time points (T24–T96) (Figure 8 and Figure
398 8- figure supplement 1). The chloroplast number per cell was constant from T4 (25 ± 8) to T24
399 (26 ± 6); however, in parallel with cell expansion (Figure 8A and B), chloroplast number
400 increased sharply (4-fold increase) between T24 (26 ± 6) and T96 (112 ± 29), indicating that
401 two rounds of chloroplast division occurred during this time. Immunoblot analysis of
402 FILAMENTOUS TEMPERATURE-SENSITIVE FtsZ1, FtsZ2-1, and FtsZ2-2 proteins showed
403 that these key components of the chloroplast division machinery were already present during
404 the early time points of de-etiolation. We observed considerably increased accumulation of
405 these proteins between T24 and T48, consistent with the idea that activation of chloroplast
406 division takes place at T24, leading the proliferation of chloroplasts (Figure 8C–D). However,
407 levels of ACCUMULATION AND REPLICATION OF CHLOROPLAST 5 (ARC5) protein,
408 another key component of the chloroplast division machinery, clearly increased during de-
409 etiolation between T8 and T12, presumably reflecting assembly of the chloroplast division
410 machinery before its activation and the proliferation of chloroplasts (Figure 8D). To test
411 whether there is a correlation between chloroplast division and either volume or developmental
412 stage, we measured the volume of dividing chloroplasts at T24 and T96 using images acquired
413 by SBF-SEM (Figure 8E and Figure 4B). The average size of dividing chloroplasts at T24 was
414 higher than the average size of all chloroplasts (96 μm^3 compared to 62 μm^3). The volume of
415 dividing chloroplasts at T96 was consistently higher than 100 μm^3 although some of the
416 chloroplasts present were smaller (Figure 8E and Figure 4B). Altogether, this indicates that
417 developing chloroplasts only divide once a certain chloroplast volume is reached.
418

419 ## Model of thylakoid surface expansion over time

420

421 During de-etiolation, thylakoid surface increased with the accumulation of galactolipids and
422 photosynthesis-related proteins, leading to the formation of functional chloroplasts. To
423 determine the thylakoid membrane surface area per seedling and its expansion over time, we
424 first calculated the surface area occupied by the main galactolipids (MGDG and DGDG) and
425 photosynthetic complexes (PSII, Cyt b_6f and PSI) per seedling (Table 2).
426 Equation 1:

427 $$Surface/seedling = nmol/seedling * N * nm^2 \ per \ molecule$$

428

429 Quantitative data for MGDG, DGDG, PsbA, PetC, and PsaC (nmol/seedling) obtained from
430 lipidomic and immunological analyses (Figures 6 and 7) were converted into number of
431 molecules/seedling using the Avogadro constant (*N*). To calculate the surface area exposed
432 to the stroma and account for the lipid double layer of the membrane, corresponding values of
433 lipids (Figure 4A) were divided by 2. In addition, the lipid values were corrected by subtracting
434 the portion of lipids incorporated into the envelope rather than present in the thylakoids (Table
435 1, Table 2 and Supplemental Dataset 3). The surface area occupied by molecules of MGDG
436 and DGDG, and that of PSII, Cyt b_6f, and PSI photosynthetic complexes (nm^2 per molecule,
437 corresponding to stroma-exposed surface) were retrieved from the literature (Table 3).
438 Specifically, we used the minimal molecular area of MGDG and DGDG (Bottier et al., 2007).
439 To quantify the surface area occupied by the galactolipids and photosynthetic complexes in
440 thylakoids per seedling, the number of molecules per seedling of galactolipids was multiplied
441 by the corresponding molecular surface area, whereas the number of molecules per seedling
442 of PsbA, PetC, and PsaC (subunits of PSII, Cyt b_6f, and PSI, respectively) were multiplied by
443 the surface area of the corresponding complex (see Table 3).
444 We calculated thylakoid surface (S) per seedling fir each time point (t) as the sum of the surface
445 occupied by MGDG, DGDG, photosynthetic complexes (PS), and ε per seedling, the latter of
446 which corresponds to compounds such as other lipids (e.g. sulfoquinovosyldiacylglycerol,
447 plastoquinone) or protein complexes (ATP synthase and NDH) that were not quantified.
448 Equation 2:

449 $$\boldsymbol{S}_thylakoid(t)/seedling = (\boldsymbol{S}_MGDG(t) + \boldsymbol{S}_DGDG(t) + \boldsymbol{S}_PS\,(t) + \varepsilon\,)/seedling$$

450

451 Omitting the unknown ε factor, we plotted the thylakoid surface calculated for each time point
452 where quantitative molecular data were available (T0, T4, T8, T12, T24, T48, T72, and T96)
453 as a function of the duration of light exposure (Figure 9- figure supplement 1). The best fitting
454 curve corresponded to a S-shaped logistic function, characterized by a lag phase at early time
455 points (T0–T8), followed by a phase of near-linear increase, and a final plateau at the final time
456 points (T72–T96). To model this function, a four-parameter logistic non-linear regression
457 equation was used to describe the dynamics of the total thylakoid surface over time (Figure 9-
458 figure supplement 1C).
459
460

461 ## Superimposition of molecular and morphometric data

462

463 We compared the values of thylakoid surface, as obtained with the model based on molecular
464 data, with the values obtained from the morphometric analysis (Figure 9). The total thylakoid

surface per seedling (S_thylakoid_morpho) was calculated by multiplying the thylakoid surface (S_thylakoid) per chloroplast obtained by morphometrics (Figure 4A) by the number of chloroplasts (nb.cp) per cell (Figure 8A) and the number of cells (nb.cells) per seedlings for each time point (t).

Equation 3:

$$\frac{\boldsymbol{S}_{thylakoid_{morpho(t)}}}{seedling} = \boldsymbol{S}_thylakoid(t)/chloroplast * nb.cp(t)/cell * nb.cells(t)/seedling$$

We estimated cell number per seedling by measuring the total volume occupied by palisade and spongy cells in cotyledons (that corresponded to 50% of total cotyledon volume) (Figure 9- figure supplement 2) and dividing this by the average cell volume quantified by Amira software (Figure 7B). As reported previously (Pyke and Leech, 1994), cell number was constant during cotyledon development. We estimated this number as 3,000 mesophyll and palisade cells per seedling at T24 and T96 (Figure 9- figure supplement 2). The thylakoid membrane surface quantified by the morphometric approach was also estimated at T4, assuming that cell number per cotyledon remained similar between T4 and T24. We compared the thylakoid surface predicted by our mathematical model to the surface estimated experimentally with our 3D thylakoid reconstruction and morphometric measurements (Figure 9 and Table 1). As shown in Figure 9, the two approaches showed very similar total thylakoid surface area per seedling at T4 and T24 and differences in this parameter by T96.

491 ## Discussion

492

493 Here, the analysis of 3D structures of entire chloroplasts in Arabidopsis in combination with
494 proteomic and lipidomic analyses provide an overview of thylakoid biogenesis. Figure 10
495 depicts a summary of the changes that occur during the de-etiolation process. When
496 considering chloroplast development, our study shows that de-etiolation is divided into two
497 phases. We documented structural changes (disassembly of the PLB and the gradual
498 formation of thylakoid lamellae) and initial increases of ER- and PL-pathway galactolipids and
499 photosynthesis-related proteins (PSII, PSI, and Cyt b_6f) during the 'Structure Establishment
500 Phase', which was followed by increased chloroplast number in parallel with cell expansion in
501 the 'Chloroplast Proliferation Phase'. Collection of quantitative data allowed us to create a
502 mathematical model of thylakoid membrane expansion and describe this process during de-
503 etiolation.

504

505 ### A set of 3D reconstructions of whole chloroplasts by SBF-SEM

506

507 In contrast to electron tomography, which is limited in the volume of observation, SBF-SEM
508 allows the acquisition of ultrastructural data from large volumes of mesophyll tissue and the
509 generation of 3D reconstructions of entire cells and chloroplasts (Figure 3 and Figure 8- figure
510 supplement 1). SEM image resolution was sufficient to visualize stromal lamellae and grana
511 contours, whereas grana segmentation in different lamellae was deduced according to our
512 own TEM analysis and literature data (Figure 2- figure supplement 1 and Figure 3- figure
513 supplement 1). This approach allowed us to obtain quantitative data of chloroplast and
514 thylakoid structure at different developmental stages during de-etiolation at the whole-
515 chloroplast level. By T96, the latest time point of our analysis, the total surface area of
516 thylakoids present in the seedling cotyledons was about 700 mm^2 (see values in Table 1 for
517 calculation), about 500-fold greater than the surface area of one cotyledon at this
518 developmental stage. This result is supported by previous estimates made regarding thylakoid
519 surface area relative to leaf surface area (Bastien et al., 2016; Demé et al., 2014). Moreover,
520 the extent of thylakoid surface area emphasizes how fast and efficient thylakoid biogenesis is
521 during plant development, allowing plants to optimize light absorption capacity, ensuring their
522 primary source of energy.

523

524 ### Chloroplast development: 'Structure Establishment Phase'

525

527 We observed TEM images and quantified 3D chloroplast ultrastructure by SBF-SEM analysis
528 during chloroplast differentiation. Typical etioplast structure of the PLB connected with tubular
529 PTs was replaced by lamellar thylakoids by T4. Measurements of PLB diameter and thylakoid
530 length and thickness were comparable with literature values (Biswal et al., 2013; Daum et al.,
531 2010; Kirchhoff et al., 2011), indicating that these morphometric values are conserved between
532 various model organisms. Thylakoid surface increased 20-fold between T4 and T24.
533 Remarkably, PSII maximum quantum yield (Fv/Fm) reached the maximal value (0.8) by T14,
534 independent of light intensity (Figure 1D and Figure 1- figure supplement 1). This shows that
535 PSII assembly, and more globally assembly of the photosynthetic machinery, occurs
536 simultaneously with thylakoid membrane formation and that photosynthesis is operational
537 almost immediately upon greening.
538 Our proteomic and lipidomic analyses suggest that chloroplast ultrastructural changes rely on
539 specifically timed molecular changes. Proteomic analysis revealed the accumulation patterns
540 of more than 5,000 unique proteins at eight time points during de-etiolation. These data provide
541 information for plastid development and more widely on light-regulated developmental
542 processes (Supplemental Dataset 1). Our dataset is more exhaustive regarding temporal
543 resolution and the number of unique proteins detected than that of previous reports on
544 chloroplast differentiation and de-etiolation (Bräutigam and Weber, 2009; Plöscher et al., 2011;
545 Reiland et al., 2011; Wang et al., 2006).
546 Here, we focused on chloroplast-localized proteins, specifically on thylakoid membrane
547 proteins. According to the SUBA4 localization consensus, 1,112 proteins were assigned to
548 plastids, which covers about a third of the total plastid proteome (Ferro et al., 2003; Hooper et
549 al., 2017; Kleffmann et al., 2007). Our data suggest that the reorganisation of pre-existing
550 molecules rather than *de novo* synthesis is responsible for the major chloroplast ultrastructural
551 changes that occur between T0 and T4. These results are consistent with other studies
552 reporting only minor increases in protein accumulation and translation during initial chloroplast
553 differentiation (Dubreuil et al., 2018; Kleffmann et al., 2007; Reiland et al., 2011). GO analysis
554 combined with expression pattern–based hierarchical clustering highlighted that most
555 photosynthesis-related proteins are globally coregulated (Figure 5- figure supplement 1,
556 clusters 2 and 6). However, targeted immunoblot analysis revealed different accumulation
557 dynamics for specific photosystem subunits: PSI subunits were detected at later time points
558 than PSII subunits, but thereafter PSI subunit accumulation was faster (Figure 6). The kinetics
559 of different photosynthetic parameters were consistent with the sequential activation of PSII
560 and PSI, in particular photochemical quenching, which showed increased oxidation of the
561 plastoquinone pool by T14 (Figure 1- figure supplement 1). Early accumulation of proteins
562 such as Lhcb5, -6, and PSBS could be a way to quickly induce photoprotective mechanisms
563 such as non-photochemical quenching to prevent PSII photodamage during initial

564 photosynthetic machinery assembly. Differences in PSI and PSII accumulation dynamics and
565 activity have been consistently observed in other chloroplast development experimental
566 systems, including in Arabidopsis cell cultures, during germination and development of
567 Arabidopsis seedlings in the light, and in tobacco leaves upon reillumination after dark
568 adaptation (Armarego-Marriott et al., 2019; Dubreuil et al., 2018; Liang et al., 2018). The
569 molecular mechanisms underlying this differential accumulation are currently unknown;
570 however, preferential localization of the PSI and PSII protein complexes in specific thylakoid
571 membrane domains (lamellae and grana, respectively) and the time taken to establish these
572 domains during chloroplast development (i.e. grana appear later than stromal lamellae) may
573 play influential roles.
574 Chloroplast membranes have a specific composition that differs from that of other cell
575 membranes. Galactolipids constitute the bulk of the thylakoid membranes, but are mostly
576 absent from other membrane systems under growth conditions where phosphorus nutrient is
577 available (Jouhet et al., 2007). MGDG and DGDG represent around 80% of the thylakoid
578 membrane lipids. The absolute quantification of 12 types of MGDG and DGDG galactolipids
579 (representing the major forms) revealed specific patterns of accumulation (Figure 7). Results
580 showed a gradual accumulation of MGDG and DGDG galactolipids derived from the ER
581 pathway from T8 to T24, whereas galactolipids from the PL pathway started to accumulate
582 after one day of light exposure (T24). This illustrates the different galactolipid compositions of
583 etioplasts and chloroplasts: ER-pathway galactolipids are predominant in the etioplast
584 whereas PL-pathway galactolipids are predominant in the chloroplast. As no significant
585 changes in lipid accumulation were observed by T4, it appears likely that the emergence of
586 PTs relies on the existing lipids in the etioplast PLB, as suggested also by Armarego-Marriott
587 et al. (2019). At later time points, galactolipids from both the ER and PL pathways constitute
588 the lipid matrix of the thylakoid membrane. How the two galactolipid biosynthesis pathways
589 are regulated during development and/or upon light treatment remains to be elucidated;
590 however, we hypothesize that the PL pathway gains traction after T24 when photosynthetic
591 capacity is fully established.
592

593 ## Chloroplast development: 'Chloroplast Proliferation Phase'

594

595 Chloroplast development continued between T24 and T96, during which thylakoid membranes
596 acquired grana stacks with more clearly defined organisation (Figure 2). Thylakoid surface
597 increased by only 41%; however, chloroplasts continued to enlarge at a rate comparable to
598 previous de-etiolation stages (T0–T24). This chloroplast volume expansion may be caused by
599 enlargement of extra-thylakoidal spaces occupied by emerging starch granules. These results

600 suggest that large amounts of lipids and proteins are necessary to build up the thylakoid
601 membrane until T24, whereas increases in lipids and proteins between T24 and T96 enable
602 the expansion of already functional thylakoid membranes in preparation for chloroplast
603 division. Indeed, chloroplast number per cell increased during de-etiolation, a process that
604 depends on the division of pre-existing chloroplasts.
605 Both chloroplasts and mitochondria divide through the activity of supramolecular complexes
606 that constitute the organelle division machineries (Yoshida, 2018). As chloroplast proliferation
607 was observed between T24 and T96, chloroplast division may correlate with developmental
608 stage of the organelle. Components of the chloroplast division machinery (e.g. FtsZ and ARC5)
609 were detectable in etioplasts; however, their protein levels accumulated significantly during de-
610 etiolation as chloroplasts proliferated (Figure 8C and D). Interestingly, the capacity to divide
611 appeared to correlate with a minimum chloroplast volume of about 100 μm^3, even at T24 when
612 most chloroplasts were smaller (Figure 8E and Figure 4B). Whether and how chloroplast size
613 and developmental stage can be sensed to activate the chloroplast division machinery remains
614 poorly understood and requires further study.
615

616 ## A model of thylakoid expansion

617

618 Our mathematical model describing the expansion of thylakoid surface per seedling over time
619 considered the surface area occupied by the membrane lipids MGDG and DGDG and the
620 major photosynthetic complexes PSII, PSI, and Cyt b_6f. We omitted some components that
621 contribute to the total thylakoid membrane surface (e.g. the protein complexes ATP synthase
622 and NDH, and the lipid sulfoquinovosyldiacylglycerol; together grouped as 'ε' in Equation 2).
623 The predictions made by our model fit the surface estimated by SBF-SEM at T4 and T24,
624 whereas they do not fit that at T96. This means that compounds used to generate the
625 mathematical model appear to contribute most to changes in thylakoid surface during early
626 stages of de-etiolation (the structure establishment phase). By contrast, during the later stages
627 of de-etiolation (the chloroplast proliferation phase), the contribution of other compounds
628 omitted in our model is obviously required to build up thylakoid surface.
629 Our proteomics data (Figure 5- figure supplement 1 and Dataset 2) revealed some proteins
630 that increased between T24 and T96, such as the FtsH protease (AT2G30950). FtsH
631 proteases have a critical function during thylakoid biogenesis. In Arabidopsis, they constitute
632 a hetero-hexameric complex of four FtsH subunits, which is integrated in the thylakoid
633 membrane (Kato and Sakamoto, 2018). Although the FtsH complex surface area is unknown
634 in Arabidopsis, it can be considered as a potential compound contributing to the thylakoid
635 surface changes missing from our mathematical model. Other proteins, such as those involved

636 in carotenoid biosynthesis (AT3G10230) or fatty acid metabolism (AT1G08640), also
637 increased significantly after T24, implying that they contribute to the 'ε' factor.
638 A follow-up study would be to test the model under different conditions to investigate how this
639 biological system responds to internal (perturbing hormone concentrations, genetic
640 modification of thylakoid lipid and protein composition) or external (different qualities of light)
641 factors. This could be instrumental in revealing new potential regulatory mechanisms of
642 thylakoid biogenesis and maintenance.
643 Upon de-etiolation, the development of photosynthetic capacity relies on successful
644 chloroplast biogenesis. At the cellular level, this process is expected to be highly coordinated
645 with the metabolism and development of other organelles. Lipid synthesis involves lipid
646 exchanges between chloroplasts and the endoplasmic reticulum. How lipid trafficking is
647 organised remains poorly understood, but could require membrane contact sites between
648 these two organelles (Michaud and Jouhet, 2019). Physical interaction between mitochondria
649 and chloroplasts have been reported previously in diatoms (Bailleul et al., 2015; Flori et al.,
650 2017). Whether such contact sites occur and are functional in plants is unknown; however,
651 these mechanisms are hypothesized to exist since it is necessary that chloroplasts exchange
652 metabolites with mitochondria and peroxisomes to ensure activation of photorespiration
653 concomitantly with photosynthesis. The study of membrane contact sites is an emerging field
654 in cell biology (Scorrano et al., 2019). Future work will focus on analysing the dynamics and
655 functionality of contact sites between chloroplast membranes and other organelles, and
656 investigate the general coordination of plant cell metabolism during de-etiolation. These
657 questions could be further addressed using the SBF-SEM stacks and proteomic resource
658 described here.

659

660 ## Materials and methods

661

662 *Plant material and Growth conditions*
663 *Arabidopsis thaliana* seeds (Columbia ecotype) were surface-sterilized with 70% (v/v) ethanol
664 with 0.05% (v/v) Triton X-100, then washed with 100% ethanol. Seeds were sown on agar
665 plates containing 0.5 × Murashige and Skoog salt mixture (Duchefa Biochemie, Haarlem,
666 Netherlands) without sucrose. Following stratification in the dark for 3 days at 4°C, seeds were
667 irradiated with 40 µmol m^{-2} s^{-1} for 2 h at 21°C and then transferred to the dark for 3 days growth
668 at 21°C. Etiolated seedlings were collected in the dark (0 h of light; T0) and at selected time
669 points (T4, T8, T12, T24, T48, T72, T96) upon continuous white light exposure (40 µmol m^{-2} s^{-}
670 ^{1} at 21°C).

671

672 *Photosynthetic parameters*

673 Maximum quantum yield of photosystem II (Φ_{MAX}= F_V/F_M =(Fm-Fo)/Fm where Fm is the maximal
674 fluorescence in dark adapted state, Fo is minimal fluorescence in dark adapted state, Fv is the
675 variable fluorescence (Fm-Fo)), photosystem II quantum yield in the light (ΦPSII), and
676 photochemical quenching (qP) were determined using a Fluorcam (Photon Systems
677 Instruments) with blue-light LEDs (470 nm). Plants were dark adapted for a minimum of 5 min
678 before measurement.

679

680 *Chlorophyll concentration*

681 Chlorophylls were extracted in 4 volumes of dimethylformamide (DMF) (v/w) overnight at 4°C.
682 After centrifugation, chlorophylls were measured using a NanoDrop™ instrument at 647 nm
683 and 664 nm. Chlorophyll contents were calculated according to previously described methods
684 (Porra et al., 1989).

685

686 *Transmission electron microscopy (TEM)*

687 Samples were fixed under vacuum (200 mBar) in 0.1 M cacodylate buffer (pH 7.4) containing
688 2.5% (w/v) glutaraldehyde and 2% (w/v) formaldehyde (fresh from paraformaldehyde) for 4 h
689 and left in the fixation solution for 16 h at 4°C. Samples were then incubated in a solution
690 containing 3% (w/v) potassium ferrocyanide and 4 mM calcium chloride in 0.1 M cacodylate
691 buffer combined with an equal volume of 4% (w/v) aqueous osmium tetroxide (OsO_4) for 1 h,
692 on ice. After the first heavy metal incubation, samples were rinsed with ddH_2O and treated with
693 1% (w/v) thiocarbohydrazide solution for 1 h at 60°C. Samples were rinsed (ddH_2O for 15 min)
694 before the second exposure to 2% (w/v) OsO_4 aqueous solution for 30 min at room
695 temperature. Following this second exposure to osmium, tissues were placed in 1% (w/v)
696 uranyl acetate (aqueous) and left overnight at 4°C. The samples were rinsed with ddH_2O for
697 15 min, and placed in the lead aspartate solution for 30 min at 60°C. Samples were dehydrated
698 in a series of aqueous ethanol solutions ranging from 50% (v/v) to 100%, then embedded in
699 Durcupan resin by successive changes of Durcupan resin/acetone mixes, with the last
700 imbibition in 100% Durcupan resin. Polymerization of the resin was conducted for 48 h at 60°C
701 (Deerinck et al., 2010). Ultra-thin sections (70 nm) were cut using Ultrathin-E microtome
702 (Reichert-Jung) equipped with a diamond knife. The sections were analysed with a Philips CM-
703 100 electron microscope operating at 60 kV.

704

705 *Confocal microscopy*

706 To derive the chloroplast and cell volumes, images of 1–5-µm thick sections of cotyledon cells
707 were acquired with X10 and X40 oil immersion objectives using a LEICA TCS SP5 confocal

laser scanning microscope. Chlorophyll was excited using a red laser (33%) and spectral detection channel was PMT3.

SBF-SEM

SBF-SEM was performed on Durcupan resin–embedded cotyledons representing the four de-etiolation time points T0, T4, T24, and T96. Overview of the mesophyll tissue (≈600 images) and zoomed stacks of the chloroplasts (≈300 images) were acquired. Voxel size of T4 zoomed stacks: 3.9 x 3.9 x 50 nm; T24: 4.7 x 4.7 x 50 nm; T96: 5.6 x 5.6 x 50 nm. Voxel size for T0 overview: 9.5 x 9.5 x 100 nm; T4: 19.3 x 19.3 x 100 nm; T24: 40 x 40 x 200 nm; T96: 43.5 x 43.5 x 200 nm.

Acquired datasets were aligned and smoothed respectively, using the plugins MultiStackReg and 3D median filter, provided by the open-source software Fiji.

We performed a stack-reslice from Fiji to generate a new stack by reconstructing the slices at a new pixel depth to obtain isotropic voxel size and improve z-resolution. The segmentation and 3D mesh geometry information of plastid /thylakoid (T0, T4, T24 and T96) were implemented by open-source software 3D Slicer (Fedorov et al., 2012) and MeshLab (Cignoni et al., 2008) respectively.

Segmentation, 3D reconstruction, and surface and volume quantification

Segmentation and 3D reconstruction of 3View and confocal images were performed using Amira software (FEI Visualization Sciences Group). Specifically, prolamellar body, thylakoids, and envelope membranes as well as the cells were selected using a semi-automatic tool called Segmentation Editor. From the segmented images, triangulated 3D surfaces were created using Generate Surface package. Quantification of morphometric data (Area 3D and volume 3D) was acquired using Label Analysis package.

Analysis of grana segmentation

Grana structures acquired from SBF-SEM were selected in Amira. The grana selections were converted in line set view in Amira software using the Generate Contour line package. To complete the grana segmentation, the line set views were imported into the Rhino 6 software (Robert McNeel & Associates, USA). Every granum was segmented in layers with a specific thickness and distance according to quantitative data collected (Figure 2- figure supplement 1 and Figure 3- figure supplement 1). After segmentation, images were re-imported in Amira software to quantify perimeter using the Label Analysis package.

745 *Chloroplast number determination*
746 Chloroplasts per cell were counted manually using Image J software (Wayne Rasband,
747 National Institutes of Health). From the same SBF-SEM stack, 5 and/or 6 cells were cropped
748 at each time point (T0, T4, T24, and T96) to quantify chloroplast number per cell. From TEM
749 images, chloroplast number/cell was determined at T24 (16 cells), T48 (12 cells), T72 (12
750 cells), and T96 (17 cells). TEM images were acquired from two independent experiments.
751
752 *Liquid chromatography–mass spectrometry analysis and protein quantification*
753 Etiolated seedlings were grown as described above. At each time point, ca. 80 seedlings were
754 pooled, frozen in liquid nitrogen, and stored at -80°C until use. Frozen material was ground
755 with a mortar and pestle, and 40–80 mg of plant material was used for protein and peptide
756 preparation using the iST kit for plant tissues (PreOmics, Germany). Briefly, each sample was
757 resuspended in 100 µL of the provided 'Lysis' buffer and processed with High Intensity
758 Focused Ultrasound (HIFU) for 1 min by setting the ultrasonic amplitude to 65% to enhance
759 solubilization. For each sample, 100 µg of protein was transferred to the cartridge and digested
760 by adding 50 µL of the provided 'Digest' solution. After 180 min of incubation at 37°C, the
761 digestion was stopped with 100 µL of the provided 'Stop' solution. The solutions in the cartridge
762 were removed by centrifugation at 3,800 *g*, whereas the peptides were retained on the iST
763 filter. Finally, the peptides were washed, eluted, dried, and re-solubilized in 18.7 µL of solvent
764 (3% (v/v) acetonitrile, 0.1% (v/v) formic acid).
765 Mass spectrometry (MS) analysis was performed on a Q Exactive HF-X mass spectrometer
766 (Thermo Scientific) equipped with a Digital PicoView source (New Objective) and coupled to a
767 M-Class UPLC (Waters). Solvent composition at the two channels was 0.1% (v/v) formic acid
768 for channel A and 0.1% formic acid, 99.9% (v/v) acetonitrile for channel B. For each sample,
769 2 µL of peptides were loaded on a commercial MZ Symmetry C18 Trap Column (100 Å, 5 µm,
770 180 µm x 20 mm, Waters) followed by nanoEase MZ C18 HSS T3 Column (100 Å, 1.8 µm, 75
771 µm x 250 mm, Waters). The peptides were eluted at a flow rate of 300 nL/min by a gradient of
772 8–27% B in 85 min, 35% B in 5 min, and 80% B in 1 min. Samples were acquired in a
773 randomized order. The mass spectrometer was operated in data-dependent mode (DDA),
774 acquiring a full-scan MS spectra (350−1400 m/z) at a resolution of 120,000 at 200 m/z after
775 accumulation to a target value of 3,000,000, followed by HCD (higher-energy collision
776 dissociation) fragmentation on the 20 most intense signals per cycle. HCD spectra were
777 acquired at a resolution of 15,000 using a normalized collision energy of 25 and a maximum
778 injection time of 22 ms. The automatic gain control (AGC) was set to 100,000 ions. Charge
779 state screening was enabled. Singly, unassigned, and charge states higher than seven were
780 rejected. Only precursors with intensity above 250,000 were selected for MS/MS. Precursor
781 masses previously selected for MS/MS measurement were excluded from further selection for

782 30 s, and the exclusion window was set at 10 ppm. The samples were acquired using internal
783 lock mass calibration on m/z 371.1012 and 445.1200. The mass spectrometry proteomics data
784 were handled using the local laboratory information management system (LIMS) (Türker et al.,
785 2010).
786 Protein quantification based on precursor signal intensity was performed using ProgenesisQI
787 for Proteomics (v4.0.6403.35451; nonlinear dynamics, Waters). Raw MS files were loaded into
788 ProgenesisQI and converted to mzIn files. To select the alignment reference, a group of
789 samples that had been measured in the middle of the run (to account for drifts in retention
790 times) and derived from de-etiolation time point T12 or later (to account for increasing sample
791 complexity) was preselected, from which replicate 3 of time point T48 was then automatically
792 chosen as best alignment reference. After automatic peak picking, precursor ions with charges
793 other than 2+, 3+, or 4+ were discarded. The five highest-ranked MS/MS spectra, at most, for
794 each peptide ion were exported, using the deisotoping and charge deconvolution option and
795 limiting the fragment ion count to 200 peaks per MS/MS. The resulting Mascot generic file
796 (.mgf) was searched with Mascot Server version 2.6.2 (www.matrixsicence.com) using the
797 following settings: trypsin digest with up to two missed cleavages allowed;
798 carbamidomethylation of cysteine as fixed modification; N-terminal acetylation and oxidation
799 of methionine residue as variable modifications; precursor ion mass tolerance 10 ppm;
800 fragment ion (MS/MS) tolerance 0.04 kDa. This search was performed against a forward and
801 reverse (decoy) Araport11 database that included common MS contaminants and iRT
802 peptides. The mascot result was imported into Scaffold Q+S (v4.8.9; Proteome Software Inc),
803 where a spectrum report was created using a false discovery rate (FDR) of 10% and 0.5% at
804 the protein and peptide level, respectively, and a minimum of one identified peptide per protein.
805 After loading the spectrum report into ProgenesisQI, samples were normalized using the
806 "normalize to all proteins" default settings (i.e. normalization was performed to all ions with
807 charges 2+, 3+ or 4+). Samples were grouped according to de-etiolation time point in a
808 between-group analysis with 4 replicates for each condition, except for time point T0 and T48,
809 where n = 3. For these two time points, one replicate each had been discarded it appeared as
810 an outlier in principal component analysis (PCA) of protein abundances between different runs
811 (Supplemental dataset 1).. Quantification employed the Hi-N method, measuring the three
812 most abundant peptides for each protein (Grossmann et al., 2010), and associated statistics
813 (q-value, PCA etc.) were calculated in ProgenesisQI. Quantification also used protein
814 grouping, which assigns proteins for which only shared but no unique peptides were identified
815 to a 'lead' identifier containing all these shared peptides and thus having the greatest coverage
816 among all grouped identifiers or highest score where coverage is equal. Quantification was
817 restricted to protein (groups) with at least two identified peptides among which at least one is
818 unique to the protein (group). Using these requirements, 5082 Arabidopsis proteins (or groups)

819 were identified. Since 13 additional identifications were exclusively associated with decoy
820 proteins, the false discovery rate at the protein level is estimated to be 0.3%. .
821
822 *Immunoblot analysis*
823 Proteins were extracted from whole seedlings in 4 volumes (w/v) of SDS-PAGE sample buffer
824 (0.2 M Tris/HCL pH 6.8, 0.4 M dithiothreitol, 8% (w/v) SDS, 0.4% (w/v) Bromophenol blue, and
825 40% (v/v) glycerol).
826 Proteins were denatured for 15 min at 65°C and cell debris were removed by centrifugation for
827 5 min at 16,000 *g*. Proteins were separated on SDS-PAGE (10–15% (w/v) polyacrylamide
828 concentrations depending on the molecular weight of the protein of interest) and transferred
829 onto a nitrocellulose membrane for immunoblotting (overnight at 4°C) in Dunn buffer (10 mM
830 $NaHCO_3$, 3 mM Na_2CO_3, 0.01% (w/v) SDS, and 20% ethanol).
831 Absolute quantification of PsbA, PetC, and PsaC was performed according to Agrisera
832 instructions and using recombinant proteins (PsbA AS01 0116S, PetC AS08 330S, and PsaC
833 AS04 042S; Agrisera, Vännäs, SWEDEN). Three respective calibration curves for the three
834 recombinant proteins were created. Concentrations used to generate the PsbA and PetC
835 calibration curves were 1.75, 2.5, 5, and 10 (ng/µL). Concentrations used to generate the PsaC
836 calibration curve were 0.375, 0.75, 1.5, and 3 (ng/µL). Immunodetections were performed
837 using specific antibodies: anti-Actin (Sigma, A0 480) at 1/3,000 dilution in 5% (w/v) milk in Tris-
838 buffered saline (TBS); anti-Lhcb2 (Agrisera, AS01 003), anti-D1(PsbA) (Agrisera, AS05 084),
839 anti-PsbO (Agrisera, AS14 2825), anti-PsbD (Agrisera, AS06 146), anti-PetC (Agrisera, AS08
840 330), and anti-AtpC (Agrisera, AS08 312) at 1/5,000 dilution in 5% milk/TBS; Anti-PsaD
841 (Agrisera, AS09 461) at 1/2,000 in 5% milk/TBS; and anti-PsaC (Agrisera, AS042P) and anti-
842 ARC5 (Agrisera, AS13 2676) at 1/2,000 in 3% (w/v) bovine serum albumin (BSA) in TBS. Anti-
843 FtsZ-1 and anti-FtsZ2-1/FtsZ 2-2 (El-Shami et al., 2002; Karamoko et al., 2011) and were used
844 at 1/2,000 dilution in 5% milk/TBS. After incubation with primary antibodies overnight at 4°C,
845 blots were washed 3 times in TBS containing 0.1% (v/v) Tween without antibodies for 10
846 minutes and incubated for 1 h at RT with horseradish peroxidase–conjugated secondary
847 antibodies (1/3,000 (v/v) anti-rabbit or anti-mouse secondary antibodies, Agrisera).
848 Chemiluminescence signals were generated with Enhanced chemiluminescence reagent (1 M
849 Tris/HCl pH 8.5, 90 mM coumaric acid, and 250 mM luminol) and detected with a Fujifilm Image
850 - Quant LAS 4000 mini CCD (GE Healthcare). Quantifications were performed with
851 ImageQuant TL software (GE Healthcare).
852
853 *Lipid profiling*
854 Lipids were extracted from whole seedlings ground in a mortar and pestle under liquid nitrogen.
855 Ground plant material corresponding to 40–80 mg fresh weight was suspended in

tetrahydrofuran:methanol (THF/MeOH) 50:50 (v/v). 10–15 glass beads (1 mm in diameter) were added followed by homogenization (3 min, 30 Hz,) and centrifugation (3 min, 14 000 *g*, at 4°C). The supernatant was removed and transferred to an HPLC vial. Lipid profiling was carried out by ultra-high pressure liquid chromatography coupled with atmospheric pressure chemical ionization-quadrupole time-of-flight mass spectrometry (UHPLC-APCI-QTOF-MS) (Martinis et al., 2011). Reverse-phase separation was performed at 60°C on an Acquity BEH C18 column (50 × 2.1 mm, 1.7 µm). The conditions were the following: solvent A = water; solvent B = methanol; 80–100% B in 3 min, 100% B for 2 min, re-equilibration at 80% B for 0.5 min. Flow rate was 0.8 ml min^{-1} and the injection volume 2.5 µl. Data were acquired using MassLynx version 4.1 (Waters), and processed with MarkerLynx XS (Waters). Peak lists consisting of variables described by mass-to-charge ratio and retention time were generated (Martinis et al., 2011; Spicher et al., 2016).

Absolute quantification of mono- (MGDG) and di-galactosyldiacylglycerol (DGDG) was conducted by creating calibration curves using MGDG (reference number 840523) and DGDG (reference number 840523) products of Avanti Company. Calibration curves were prepared using the following concentrations: 0.08, 0.4, 2, 10, and 50 µg ml^{-1} of MGDG or DGDG.

Mathematical Model

A non-linear mixed effects model (with fixed effect of time and random effect of replicates on 3 of the parameters), built on a 4-parameter logistic function, was implemented in R (free software created by Ross Ihaka and Robert Gentleman, Auckland University, New Zealand), following the examples in Pinheiro and Bates (2000). The R-packages used are: nlme (Pinheiro and Bates, 2000), effects, lattice and car (Fox and Weisberg, 2018). To account for self-correlation at the replicate level, we proceeded to fit an overall mixed-effects model to the data (package 'nlme' from R), using the replicate's as random effect term (Figure 9_supplement 1). The four parameters *a, b, c* and *d* have been calculated (Figure 9_supplement 1) and the three plots (one for each biological replicate) (Figure 9_supplement 1) indicated the fitting curve for a series of data points.

Acknowledgements

This work was supported by the University of Neuchâtel and ETH Zurich, a grant from the Swiss National Science Foundation (3100A0-112638) to E.D., and grants 31003A_156998 and 31003A_176191 to F.K.. We thank Jonas Grossmann, Laura Kunz and Paolo Nanni from the Functional Genomic Center Zurich (FGCZ) for peptide preparation for mass spectrometry, acquisition of the raw data and help with associated data analysis, the ETH Zurich microscopy

892 facility (ScopeM) for advice in conducting SBF-SEM analysis. We thank Slobodeanu Radu
893 Alexandru and Federico Giacomarra for help with bioinformatics analysis, and Romain Bessire
894 for help with image processing software. We thank Roman Ulm and Michel Goldschmidt-
895 Clermont for critical reading of the manuscript.
896
897 **Author contributions**
898 Conceptualization, R.P., T.P., S.Z., F.K., and E.D.; Investigation, R.P., S.E., B.P., D.F., C.U.,
899 G.G., and E.D.; Writing R.P, B.P., F.K. and E.D.; Supervision, F.K. and E.D.
900
901 **Competing interests**
902 The authors declare no competing interests.
903

904 Figure Legends

905 **Figure 1: Photosynthesis onset during de-etiolation.** (A) Scheme of the experimental
906 design. Seeds of *Arabidopsis thaliana* (Columbia) sown on agar plates were stratified for three
907 days at 4°C and then transferred to 22°C in the dark. After three days, etiolated seedlings were
908 exposed to continuous white light (40 µmol/m^2/s) and harvested at different time points during
909 de-etiolation. Selected time points used for different analyses are indicated. (B) Cotyledon
910 phenotype of etiolated seedlings (T0) after 4 h (T4), 24 h (T24), and 96 (T96) h in continuous
911 white light. Scale bars: 0.5 mm. (C) Chlorophyll quantification at different time points upon
912 illumination. Error bars indicate ± SD (n=3). (D) Maximum quantum yield of photosystem II
913 (Fv/Fm). Error bars indicate ± SD (n=4–10). For some data points, the error bars are inferior
914 to the size of the symbol. Measurements of further photosynthetic parameters are presented
915 in Figure 1- figure supplement 1.
916
917 **Figure 2: Qualitative analysis of chloroplast ultrastructure during de-etiolation**.
918 Transmission electron microscopy (TEM) images of cotyledon cells of 3-day-old, dark-grown
919 *Arabidopsis thaliana* (Columbia) seedlings illuminated for 0 h (A and E), 4 h (B and F), 24 h (C
920 and G), and 96 h (D and H) in continuous white light (40 µmol/m^2/s). (A–D) Scale bars: 500
921 nm, (E–H) higher magnification of A–D images; Scale bars: 200 nm. PLB: prolamellar body;
922 PT: prothylakoid; PE: plastid envelope; SG: starch grain; GS: grana stack; SL: single lamella.
923 Specific details for measurements of lamella thickness are provided in Figure 2- figure
924 supplement 1.
925
926 **Figure 3: 3D reconstructions of chloroplast thylakoid network during de-etiolation.** (A–
927 D) Scanning electron microscopy (SEM) micrographs of representative etioplasts and

928 chloroplasts from 3-day-old, dark-grown *Arabidopsis thaliana* seedlings illuminated for 0 h (T0;
929 A), 4 h (T4; B), 24 h (T24; C), and 96 h (T96; D) in continuous white light (40 µmol/m^2/s). (E–
930 H) Partial 3D reconstruction of thylakoid membranes (green) and envelope (blue) at T0 (E), T4
931 (F), T24 (G) and T96 (H). Z-depth of thylakoid membrane reconstruction corresponds to 0.06
932 µm (E), 0.10 µm (F), 0.13 µm (G), and 0.15 µm (H). (I–N). 3D reconstruction of a thylakoid
933 membrane of an etioplast at T0 (I) or a chloroplast at T4 (L), T24 (M), and T96 (N). Scale bars
934 = 1 µm. Details of grana segmentation at T24 are provided in Figure 3- figure supplement 1.
935
936 **Figure 4: Quantitative analysis of chloroplast volume and thylakoid surface during de-**
937 **etiolation.** Quantification of thylakoid surface per chloroplast (A) and chloroplast volume (B)
938 using 3-day-old, dark-grown *Arabidopsis thaliana* (Columbia) seedlings illuminated for 0 h, 4
939 h, 24 h, and 96 h in continuous white light (40 µmol/m^2/s). Morphometric data were quantified
940 by Labels analysis module of Amira software. Error bars indicate ± SD (n=3). The total
941 thylakoid surface indicated in A corresponds to the thylakoid surface exposed to the stroma,
942 calculated in Amira software, in addition to the percentage of the grana surface (%Gs)
943 calculated as described in Figure 3- figure supplement 1.
944
945 **Figure 5: Accumulation dynamics of plastid proteins during de-etiolation**. 3-day-old
946 etiolated seedlings of *Arabidopsis thaliana* were illuminated for 0 h (T0), 4 h (T4), 8 h (T8), 12
947 h (T12), 24 h (T24), 48 h (T48), 72 h (T72), and 96 h (T96) under white light (40 µmol/m^2/s).
948 Hierarchical clustering (Euclidean, average linkage) of normalized protein abundance for
949 photosynthesis-(A), galactolipid metabolism- (B), chlorophyll metabolism- (C), and protein
950 import-related proteins during de-etiolation (D). Protein abundance was quantified by shot-gun
951 proteomics and heatmap colors indicate the fold change (average of 3–4 replicates) of each
952 selected protein at each time point of de-etiolation (T0 to T96), relative to the last time point
953 (T96). Note that some PORA values in panel D were higher than 3.5 and outside of the color
954 range limits. Further hierarchical clustering based on the accumulation dynamics of all plastid-
955 localized proteins is provided in Figure 5- figure supplement 1.
956
957 **Figure 6: Accumulation dynamics of photosynthesis-related proteins during de-**
958 **etiolation.** 3-day-old etiolated seedlings of *Arabidopsis thaliana* were illuminated for 0 h (T0),
959 4 h (T4), 8 h (T8), 12 h (T12), 24 h (T24), 48 h (T48), 72 h (T72), and 96 h (T96) under white
960 light (40 µmol/m^2/s). (A) Proteins were separated by SDS-PAGE and transferred onto
961 nitrocellulose membrane and immunodetected with antibodies against PsbA, PsbD, PsbO,
962 PetC, PsaD, PsaC, Lhcb2, AtpC, ELIP, POR proteins. (B–C) Quantification of PsbA, PetC,
963 and PsaC during de-etiolation. Heatmap (B) was generated after normalization of the amount
964 of each protein relative to the last time point (T96). Graph (C) corresponds to the absolute

quantification of proteins at T96. Error bars indicate ± SD (n=3). Quantification of photosystem-related proteins during de-etiolation is detailed in Figure 6- figure supplement 1.

Figure 7: Accumulation dynamics of galactolipids during de-etiolation. 3-day-old etiolated seedlings of *Arabidopsis thaliana* were illuminated for 0 h (T0), 4 h (T4), 8 h (T8), 12 h (T12), 24 h (T24), 48 h (T48), 72 h (T72), and 96 h (T96) under white light (40 µmol/m^2/s). (A) Heatmap representation of galactolipids (MGDG and DGDG) during de-etiolation. Samples were normalized to the last time point (T96). (B) Absolute quantification at T96 expressed in nmol/seedling. Error bars indicate ± SD (n=4). (C) Absolute quantification (nmol/seedling) of the most abundant chloroplast galactolipids MGDG (MGDG 18:3/18:3, MGDG 18:3/16:3, MGDG 18:3/16:1) and DGDG (DGDG 18:3/18:3, DGDG 18:3/16:0) at different time points during de-etiolation. Error bars indicate ± SD (n=4). (D) The MGDG/DGDG ratio was calculated using all 12 species of galactolipids detected during de-etiolation. Error bars indicate ± SD (n=4).

Figure 8: Relationship between chloroplast proliferation and chloroplast volume. (A-B) Chloroplast number and cell volume in cotyledons of 3-day-old, dark-grown *Arabidopsis thaliana* seedlings illuminated for 0 h (T0), 4 h (T4), 24 h (T24), and 96 h (T96) in continuous white light (40 µmol/m^2/s). (A) Chloroplast number per cell during de-etiolation. Error bars indicate ± SD (n=6 for T0 and T7; 7 for T24; 5 for T96). (B) Cell volume was quantified by the Labels analysis module of Amira software. Error bars indicate ± SD (n=5–6). (C–D) Total proteins were extracted from T0–T96 seedlings, separated on SDS-PAGE, and transferred onto nitrocellulose. Proteins involved in plastid division (C, FtsZ; D, ARC5) and loading control (actin) were detected using specific antibodies (FtsZ2 antibody recognizes both FtsZ2-1 and FtsZ2-2). (E) Volume of dividing chloroplast at T24 and T96. Error bars indicate ± SD (n=3). Further details of chloroplast proliferation in parallel with cell expansion are provided in Figure 8- figure supplement 1.

Figure 9: Superimposition of thylakoid surface per seedling obtained from morphometric analysis and mathematical modeling. Thylakoid surface per seedling was estimated using quantitative data from 3View analysis ('MORPHO' black dots at T4, T24, and T96; and see Figure 4 and Table 1) and model generated using the quantitative data from proteomics and lipidomics ('MODEL' red line at T0, T4, T8, T12, T24, T48, T72, and T96, and Table 1). Further details are provided in Figure 9- figure supplement 1 and 2.

1002 **Figure 10: Overview of changes observed during the de-etiolation process**
1003 **in *Arabidopsis thaliana* seedlings.** The 'Structure Establishment Phase' is correlated with
1004 disassembly of the PLB and gradual formation of the thylakoid membrane as well as an initial
1005 increase of eukaryotic (after 8 h) and prokaryotic (after 24 h) galactolipids and photosynthesis-
1006 related proteins (PSII subunits at 4 h, PSI and cyt b_6f at 12 h). The subsequent 'Chloroplast
1007 Proliferation Phase' is associated with an increase in chloroplast number in concomitance with
1008 cell expansion, a linear increase of prokaryotic and eukaryotic galactolipids and
1009 photosynthesis-related proteins, and increased grana stacking. The red curve (retrieved from
1010 the Figure 9) shows thylakoid surface/seedling dynamics during the de-etiolation process.
1011
1012
1013 **TABLE 1: Collection of quantitative data.** Morphometric data corresponding to thylakoid
1014 surfaces and volumes, thylakoid/envelope surface ratio, and chloroplast and cell volumes were
1015 collected after 3View analysis. Chloroplast and cell volumes were also quantified by
1016 subsequent confocal microscopy analysis, whereas plastid length was measured using TEM
1017 images. Molecular data for galactolipids (GLs) were analysed by lipidomics, whereas PsbA,
1018 PsaC, and PetC were quantified by quantitative immunodetection.
1019
1020 **TABLE 2: Surface area occupied by the main galactolipids (MGDG and DGDG) and**
1021 **photosynthetic complexes (PSII, cyt b_6f, and PSI).** Shown are values at different time points
1022 following illumination of 3-day-old etiolated seedlings. Each value (in bold) indicates the
1023 calculated surface area in μm^2 and corresponds to the average of three biological replicates.
1024 Errors indicate SD.
1025
1026 **TABLE 3: Surface area occupied by galactolipid and photosynthetic complexes**. (A)
1027 Values were retrieved from the corresponding references. MGDG and DGDG surfaces
1028 correspond to the minimal molecular area. The surfaces of PSII-LHCII, PSI, and Cyt b_6f
1029 complexes correspond to the surface exposed to the stroma (19*26 nm, 20*15 nm, and 90*55
1030 Å, respectively). (B) Values from the table in panel A were used to calculate the total surface
1031 per seedling corresponding to MGDG and DGDG galactolipids, and PSII, PSI, and Cyt b_6f
1032 complexes.
1033
1034
1035
1036

1037 ## Figure Supplements

1038 **Figure 1- figure supplement 1: Photosynthesis parameters during de-etiolation.**
1039 Maximum photosynthetic quantum yield of PSII (Fv/Fm) of plants (dark-adapted for 5 minutes)
1040 grown under different light intensities (A). Photochemical quenching (B) and efficiency of the
1041 photosystem PSII (Φ PSII; C) measurements were made on 3-day-old etiolated seedlings that
1042 were de-etiolated under continuous light (40 µmol/m^2/s) using a Fluorcam (Photon System
1043 Instrument). Error bars indicate ± SD (n=10).
1044

1045 **Figure 2- figure supplement 1: Measurement of lamella thickness.** (A) TEM chloroplast
1046 micrographs of 3-day-old, dark-grown *Arabidopsis thaliana* (Columbia) seedlings illuminated
1047 for 96 h in continuous white light (40 µmol/m^2/s) were used to measure the thickness of
1048 lamellae that constitute the grana stack. Measurements were performed using ImageJ. Scale
1049 bar: 100 nm. (B) Equation used to calculate the thickness of one lamella. (C) Data indicate
1050 mean ± SD (n=10 for 2 lamellae and n=7 for 3 lamellae).
1051

1052 **Figure 4- figure supplement 1: Grana segmentation (T24).** (A) Selection of thylakoid
1053 membrane exposed to the stroma was acquired using Amira. (B) The perimeter of the grana
1054 structures showed in black were segmented in layers of a specific thickness and distance using
1055 Rhino software, with the corresponding thickness (lamellae and stromal gap) measured and
1056 calculated as described in Figure 2- figure supplement 1. Grana segmentation was performed
1057 using thylakoid membrane of de-etiolating seedlings exposed to continuous white light (40
1058 µmol/m^2/s) for 24 (T24) and 96 (T96) h. A representative example of a T24 replicate is
1059 illustrated here. (C) Schematic representation of the grana stack perimeter comprising
1060 margins, end membranes, and intergranal lamellae. (D) Equation used to calculate the
1061 percentage of the grana stack surface area relative to total thylakoid surface area.
1062

1063 **Figure 5- figure supplement 1: Accumulation dynamics of selected plastid proteins**
1064 **during de-etiolation.** Hierarchical clustering (Euclidean, average linkage) of normalized
1065 protein abundance (log2 fold changes) for plastid-localized proteins during de-etiolation.
1066 Normalization was performed to the last time point (96 h). Defined clusters are indicated with
1067 different colours (1= purple; 2= pink; 3=turquoise; 4= brown; 5 = light green; 6 = dark green).
1068 Protein IDs (AGI) and names are legible upon zoom-in.
1069

1070 **Figure 6- figure supplement 1: Quantification of photosynthesis-related proteins.** (A)
1071 Immunodetection of PsbA, PetC, and PsaC during de-etiolation. Dilutions were used for the
1072 later time points to avoid saturation of the signal. (B) Different bands were detected by
1073 Amersham Imager program and quantified by Image QuantTL (Amersham). (C) Calibration

1074 curves were created using recombinant proteins (Agrisera). Calibration curve composition:
1075 PsbA 10 ng (A; lane a), 5 ng (b), 2.5 ng (c), and 1.25 ng (d); PetC 10 ng (e), 5 ng (f), 2.5 ng
1076 (g), and 1.25 ng (h); PsaC 3 ng (i), 1.5 ng (l), 0.75 ng (m), and 0.325 ng (n). The analysis was
1077 carried out on 3–4 independent experiments (BIO1–4).
1078
1079 **Figure 8- figure supplement 1. Chloroplast proliferation in parallel with cell expansion.**
1080 SEM micrographs of 3-day-old, dark-grown *Arabidopsis thaliana* (Columbia) seedlings
1081 illuminated for 0 h (T0; A), 4 h (T4; B), 24 h (T24; C), and 96 h (T96; D) in continuous white
1082 light (40 µmol/m^2/s). Palisade (PA) and spongy (SP) cells are indicated. Scale bars: 15 µm.
1083 (E) 3D reconstruction of a palisade cell at T24 after segmentation of chloroplasts and cell
1084 plasma membrane. (F–I) Confocal images of cotyledons of dark-grown seedlings at T24 (F),
1085 T48 (G), T72 (H), and T96 (I). Scale bars: 10 µm. (L–O) TEM micrographs of cotyledon cells
1086 of dark-grown seedlings at T24 (L), T48 (M), T72 (N), and T96 (O). L–M, scale bars: 2 µm; N–
1087 O, scale bars: 5 µm. (P) Cell perimeter measured with Amira software using (red line). The Z-
1088 depth of each stack corresponds to 1 µm. Relative chloroplast number per cell was counted
1089 using 2D TEM images (black line). Red error bars indicate ± SD (n= 17). Black error bars
1090 indicate ± SD (n= 3–4). (Q) Box plots of single chloroplast total volume quantified at T48 and
1091 T72. Each box corresponds to the distribution of a chloroplast population analysed using
1092 confocal and SBF-SEM stacks. n=66 (T48); 62 (T72).
1093

1094
1095 **Figure 9- figure supplement 1: Non-linear mixed effect model of thylakoid surface**
1096 **during de-etiolation.** (A) Total surface of thylakoid membrane components (in µm^2) in function
1097 of de-etiolation time point. (B) Individual plots for each biological replicate. (C) Values, standard
1098 errors, t-value, and P-value of the four parameters (a, b, c, and d) used in the main equation.
1099 Smodel = surface of thylakoid at a specific time (t)
1100 t = time of light exposure (h)
1101 a = asymptote (to the left if c>0)
1102 b= right asymptote (to the right if c>0)
1103 c= proportional to the slope of the curve at the inflection point
1104 d= inflection point (point at which the mean Smodel value is reached)
1105
1106
1107 **Figure 9- figure supplement 2: Morphometric analysis of cotyledons.** (A) Cotyledon
1108 surface area of 3-day-old, dark-grown *Arabidopsis thaliana* (Columbia) seedlings illuminated
1109 with 24 h (T24) and 96 h (T96) of continuous white light (40 µmol/m^2/s). (B) The thickness (T)

1110 of mesophyll tissue constituted of palisade (PA), spongy (SP) cells, and vascular system (VS)
1111 in addition to the epidermal tissue was measured. Error bars indicate ± SD (n=4). (C)
1112 Estimation of cotyledon volume. Error bars indicate ± SD (n=3). (D) Estimation of the number
1113 of cells per cotyledon (see Supplemental Dataset 4 for calculations)
1114
1115

1116 # References

1117 Agne B, Kessler F. 2010. Modifications at the A-domain of the chloroplast import receptor
1118 Toc159. *Plant Signal Behav* **5**:1513–6. doi:10.1104/pp.110.158048

1119 Amunts A, Nelson N. 2009. Plant Photosystem I Design in the Light of Evolution. *Structure*
1120 **17**:637–650. doi:10.1016/j.str.2009.03.006

1121 Armarego-Marriott T, Kowalewska Ł, Burgos A, Fischer A, Thiele W, Erban A, Strand D,
1122 Kahlau S, Hertle A, Kopka J, Walther D, Reich Z, Schöttler MA, Bock R. 2019. Highly
1123 Resolved Systems Biology to Dissect the Etioplast-to-Chloroplast Transition in Tobacco
1124 Leaves. *Plant Physiol* **180**:654–681. doi:10.1104/pp.18.01432

1125 Aronsson H, Schöttler M a, Kelly A a, Sundqvist C, Dörmann P, Karim S, Jarvis P. 2008.
1126 Monogalactosyldiacylglycerol deficiency in Arabidopsis affects pigment composition in
1127 the prolamellar body and impairs thylakoid membrane energization and photoprotection
1128 in leaves. *Plant Physiol* **148**:580–592. doi:10.1104/pp.108.123372

1129 Austin JR, Staehelin LA. 2011. Three-Dimensional Architecture of Grana and Stroma
1130 Thylakoids of Higher Plants as Determined by Electron Tomography. *Plant Physiol*
1131 **155**:1601–1611. doi:10.1104/pp.110.170647

1132 Bailleul B, Berne N, Murik O, Petroutsos D, Prihoda J, Tanaka A, Villanova V, Bligny R, Flori
1133 S, Falconet D, Krieger-Liszkay A, Santabarbara S, Rappaport F, Joliot P, Tirichine L,
1134 Falkowski PG, Cardol P, Bowler C, Finazzi G. 2015. Energetic coupling between plastids
1135 and mitochondria drives CO2 assimilation in diatoms. *Nature* **524**:366–369.
1136 doi:10.1038/nature14599

1137 Bastien O, Botella C, Chevalier F, Block MA, Jouhet J, Breton C, Girard-Egrot A, Maréchal E.
1138 2016. New Insights on Thylakoid Biogenesis in Plant Cells, International Review of Cell
1139 and Molecular Biology. Academic Press. doi:10.1016/bs.ircmb.2015.12.001

1140 Bauer J, Chen K, Hiltbunner a, Wehrli E, Eugster M, Schnell D, Kessler F. 2000. The major
1141 protein import receptor of plastids is essential for chloroplast biogenesis. *Nature* **403**:203–
1142 7. doi:10.1038/35003214

1143 Bischof S, Baerenfaller K, Wildhaber T, Troesch R, Vidi P-A, Roschitzki B, Hirsch-Hoffmann
1144 M, Hennig L, Kessler F, Gruissem W, Baginsky S. 2011. Plastid proteome assembly
1145 without Toc159: photosynthetic protein import and accumulation of N-acetylated plastid
1146 precursor proteins. *Plant Cell* **23**:3911–28. doi:10.1105/tpc.111.092882

1147 Biswal B, Krupinska K, Biswal U. 2013. Plastid Development in Leaves during Growth and
1148 Senescence. doi:10.1007/978-94-007-5724-0

1149 Block MA, Dorne A-J, Joyard J, Douce R. 1983. Preparation and Characterization of
1150 Membrane Fractions of Outer and Inner Envelope Membranes from Spinach C. *J Biol*
1151 *Chem* **258**:13281–13286. doi:10.1007/978-94-017-4973-2_5

1152 Blomqvist LA, Ryberg M, Sundqvist C. 2008. Proteomic analysis of highly purified prolamellar
1153 bodies reveals their significance in chloroplast development. *Photosynth Res* **96**:37–50.
1154 doi:10.1007/s11120-007-9281-y

1155 Bottier C, Géan J, Artzner F, Desbat B, Pézolet M, Renault A, Marion D, Vié V. 2007.
1156 Galactosyl headgroup interactions control the molecular packing of wheat lipids in
1157 Langmuir films and in hydrated liquid-crystalline mesophases. *Biochim Biophys Acta*
1158 **1768**:1526–1540. doi:10.1016/j.bbamem.2007.02.021

1159 Bräutigam A, Weber APM. 2009. Proteomic analysis of the proplastid envelope membrane
1160 provides novel insights into small molecule and protein transport across proplastid
1161 membranes. *Mol Plant* **2**:1247–1261. doi:10.1093/mp/ssp070

1162 Caffarri S, Tibiletti T, Jennings R, Santabarbara S. 2014. A Comparison Between Plant
1163 Photosystem I and Photosystem II Architecture and Functioning. *Curr Protein Pept Sci*
1164 **15**:296–331. doi:10.2174/1389203715666140327102218

1165 Chen Y-E, Ma J, Wu N, Su Y-Q, Zhang Z-W, Yuan M, Zhang H-Y, Zeng X-Y, Yuan S. 2018.
1166 The roles of Arabidopsis proteins of Lhcb4, Lhcb5 and Lhcb6 in oxidative stress under
1167 natural light conditions. *Plant Physiol Biochem* **130**:267–276.
1168 doi:https://doi.org/10.1016/j.plaphy.2018.07.014

1169 Cignoni P, Callieri M, Corsini M, Dellepiane M, Ganovelli F, Ranzuglia G. 2008. MeshLab: An
1170 open-source mesh processing tool. *6th Eurographics Ital Chapter Conf 2008 - Proc* 129–
1171 136. doi:10.2312/LocalChapterEvents/ItalChap/ItalianChapConf2008/129-136

1172 Daum B, Kühlbrandt W. 2011. Electron tomography of plant thylakoid membranes. *J Exp Bot*
1173 **62**:2393–2402. doi:10.1093/jxb/err034

1174 Daum B, Nicastro D, Mcintosh JR, Ku W. 2010. Arrangement of Photosystem II and ATP
1175 Synthase in Chloroplast Membranes of Spinach and Pea 1299–1312.
1176 doi:10.1105/tpc.109.071431

1177 Deerinck TJ, Bushong EA, Thor A, Ellisman MH. 2010. NCMIR methods for 3D EM : a new
1178 protocol for preparation of biological specimens for serial block face scanning electron
1179 microscopy 6–8.

1180 Demarsy E, Lakshmanan AM, Kessler F. 2014. Border control: selectivity of chloroplast protein
1181 import and regulation at the TOC-complex. *Front Plant Sci* **5**:483.
1182 doi:10.3389/fpls.2014.00483

1183 Demé B, Cataye C, Block M a, Maréchal E, Jouhet J. 2014. Contribution of galactoglycerolipids
1184 to the 3-dimensional architecture of thylakoids. *FASEB J* **28**:3373–83. doi:10.1096/fj.13-
1185 247395

1186 Dubreuil C, Jin X, Barajas-López J de D, Hewitt TC, Tanz SK, Dobrenel T, Schröder WP,
1187 Hanson J, Pesquet E, Grönlund A, Small I, Strand \r Asa. 2018. Establishment of
1188 Photosynthesis through Chloroplast Development Is Controlled by Two Distinct
1189 Regulatory Phases. *Plant Physiol* **176**:1199–1214. doi:10.1104/pp.17.00435

1190 El-Shami M, El-Kafafi S, Falconet D, Lerbs-Mache S. 2002. Cell cycle-dependent modulation
1191 of FtsZ expression in synchronized tobacco BY2 cells. *Mol Genet Genomics* **267**:254–
1192 261. doi:10.1007/s00438-002-0660-y

1193 Engel BD, Schaffer M, Cuellar LK, Villa E, Plitzko JM, Baumeister W. 2015. Native architecture
1194 of the chlamydomonas chloroplast revealed by in situ cryo-electron tomography. *Elife*
1195 **2015**:1–29. doi:10.7554/eLife.04889

1196 Fedorov A, Beichel R, Kalpathy-Cramer J, Finet J, Fillion-Robin J-C, Pujol S, Bauer C,
1197 Jennings D, Fennessy F, Sonka M, Buatti J, Aylward S, Miller J V, Pieper S, Kikinis R.
1198 2012. 3D Slicer as an image computing platform for the Quantitative Imaging Network.
1199 *Magn Reson Imaging* **30**:1323–1341. doi:https://doi.org/10.1016/j.mri.2012.05.001

1200 Ferro M, Salvi D, Brugière S, Miras S, Kowalski S, Louwagie M, Garin J, Joyard J, Rolland N.
1201 2003. Proteomics of the chloroplast envelope membranes from Arabidopsis thaliana. *Mol*
1202 *Cell Proteomics* **2**:325–345. doi:10.1074/mcp.M300030-MCP200

1203 Flori S, Jouneau P-H, Bailleul B, Gallet B, Estrozi LF, Moriscot C, Bastien O, Eicke S, Schober
1204 A, Bártulos CR, Maréchal E, Kroth PG, Petroutsos D, Zeeman S, Breyton C, Schoehn G,
1205 Falconet D, Finazzi G. 2017. Plastid thylakoid architecture optimizes photosynthesis in
1206 diatoms. *Nat Commun* **8**:15885. doi:10.1038/ncomms15885

1207 Fox J, Weisberg S. 2018. Visualizing fit and lack of fit in complex regression models with

1208 predictor effect plots and partial residuals, Journal of Statistical Software.
1209 doi:10.18637/jss.v087.i09

1210 Grossmann J, Roschitzki B, Panse C, Fortes C, Barkow-Oesterreicher S, Rutishauser D,
1211 Schlapbach R. 2010. One master protein that is identified by a set of peptides that are
1212 not included (all together) in any other protein group. All proteins that are identified by the
1213 same set or a subset of those peptides. *J Proteomics* **73**:1740–1746.
1214 doi:doi.org/10.1016/j.jprot.2010.05.011

1215 Hashimoto M, Endo T, Peltier G, Tasaka M, Shikanai T. 2003. A nucleus-encoded factor,
1216 CRR2, is essential for the expression of chloroplast ndhB in Arabidopsis. *Plant J* **36**:541–
1217 549. doi:10.1046/j.1365-313X.2003.01900.x

1218 Hooper CM, Castleden IR, Tanz SK, Aryamanesh N, Millar AH. 2017. SUBA4: The interactive
1219 data analysis centre for Arabidopsis subcellular protein locations. *Nucleic Acids Res*
1220 **45**:D1064–D1074. doi:10.1093/nar/gkw1041

1221 Jouhet J, Marechal E, Block MA. 2007. Glycerolipid transfer for the building of membranes in
1222 plant cells. *Prog Lipid Res* **46**:37–55. doi:10.1016/j.plipres.2006.06.002

1223 Karamoko M, El-Kafafi ES, Mandaron P, Lerbs-Mache S, Falconet D. 2011. Multiple FtsZ2
1224 isoforms involved in chloroplast division and biogenesis are developmentally associated
1225 with thylakoid membranes in Arabidopsis. *FEBS Lett* **585**:1203–1208.
1226 doi:10.1016/j.febslet.2011.03.041

1227 Kato Y, Sakamoto W. 2018. FtsH protease in the thylakoid membrane: Physiological functions
1228 and the regulation of protease activity. *Front Plant Sci* **9**:1–8. doi:10.3389/fpls.2018.00855

1229 Kessler F, Schnell DJ. 2006. The function and diversity of plastid protein import pathways: A
1230 multilane GTPase highway into plastids. *Traffic* **7**:248–257. doi:10.1111/j.1600-
1231 0854.2005.00382.x

1232 Kimura M, Manabe K, Abe T, Yoshida S, Matsui M, Yamamoto YY. 2003. Analysis of Hydrogen
1233 Peroxide–independent Expression of the High-light–inducible ELIP2 Gene with the Aid of
1234 the ELIP2 Promoter–Luciferase Fusion¶. *Photochem Photobiol* **77**:668–674.
1235 doi:10.1562/0031-8655(2003)0770668AOHPEO2.0.CO2

1236 Kirchhoff H, Hall C, Wood M, Herbstová M, Tsabari O, Nevo R, Charuvi D, Eyal S, Ziv R. 2011.
1237 Dynamic control of protein diffusion within the granal thylakoid lumen **108**:20248–20253.
1238 doi:10.1073/pnas.1104141109

1239 Kleffmann T, von Zychlinski A, Russenberger D, Hirsch-Hoffmann M, Gehrig P, Gruissem W,
1240 Baginsky S. 2007. Proteome Dynamics during Plastid Differentiation in Rice. *Plant*
1241 *Physiol* **143**:912 LP – 923. doi:10.1104/pp.106.090738

1242 Kobayashi K. 2016. Role of membrane glycerolipids in photosynthesis, thylakoid biogenesis
1243 and chloroplast development. *J Plant Res* **129**:565–580. doi:10.1007/s10265-016-0827-
1244 y

1245 Koochak H, Puthiyaveetil S, Mullendore DL, Li M, Kirchhoff H. 2019. The structural and
1246 functional domains of plant thylakoid membranes. *Plant J* **97**:412–429.
1247 doi:10.1111/tpj.14127

1248 Kowalewska ŁM, Mazur R, Suski S, Garstka M, Mostowska A. 2016. Three-dimensional
1249 visualization of the internal plastid membrane network during runner bean chloroplast
1250 biogenesis. Dynamic model of the tubular-lamellar transformation. *Plant Cell* **28**:875–891.
1251 doi:10.1105/tpc.15.01053

1252 Kubis S, Baldwin A, Patel R, Razzaq A, Dupree P, Lilley K, Kurth J, Leister D, Jarvis P. 2003.
1253 The Arabidopsis ppi1 mutant is specifically defective in the expression, chloroplast import,
1254 and accumulation of photosynthetic proteins. *Plant Cell* **15**:1859–1871.
1255 doi:10.1105/tpc.012955

1256 Kurisu G, Zhang H, Smith JL, Cramer WA. 2003. Structure of the Cytochrome b 6 f Complex
1257 of Oxygenic Photosynthesis : Tuning the Cavity **302**:1009–1015.
1258 doi:10.1126/science.1090165

1259 Li XP, Björkman O, Shih C, Grossman AR, Rosenquist M, Jansson S, Niyogi KK. 2000. A
1260 pigment-binding protein essential for regulation of photosynthetic light harvesting. *Nature*
1261 **403**:391–395. doi:10.1038/35000131

1262 Liang Z, Zhu N, Mai KK, Liu Z, Tzeng D, Osteryoung KW. 2018. Thylakoid-Bound Polysomes
1263 and a Dynamin-Related Protein , FZL , Mediate Critical Stages of the Linear Chloroplast
1264 Biogenesis Program in Greening Arabidopsis Cotyledons **30**:1476–1495.
1265 doi:10.1105/tpc.17.00972

1266 Marechal E, Block MA, Dome A, Douce R, Joyard J. 1997. Lipid synthesis and metabolism in
1267 the plastid envelope **100**:65–77. doi:10.1111/j.1399-3054.1997.tb03455.x

1268 Martinis J, Kessler F, Glauser G. 2011. A novel method for prenylquinone profiling in plant
1269 tissues by ultra-high pressure liquid chromatography-mass spectrometry. *Plant Methods*

1270 **7**:1–23. doi:10.1186/1746-4811-7-23

1271 Mazur R, Mostowska A, Szach J, Gieczewska K, Wójtowicz J, Bednarska K, Garstka M,
1272 Kowalewska Ł. 2019. Galactolipid deficiency disturbs spatial arrangement of the thylakoid
1273 network in Arabidopsis thaliana plants. *J Exp Bot* **70**:4689–4703. doi:10.1093/jxb/erz219

1274 Mi H, Muruganujan A, Huang X, Ebert D, Mills C, Guo X, Thomas PD. 2019. Protocol Update
1275 for large-scale genome and gene function analysis with the PANTHER classification
1276 system (v.14.0). *Nat Protoc* **14**:703–721. doi:10.1038/s41596-019-0128-8

1277 Michaud M, Jouhet J. 2019. Lipid Trafficking at Membrane Contact Sites During Plant
1278 Development and Stress Response. *Front Plant Sci* **10**:1–10.
1279 doi:10.3389/fpls.2019.00002

1280 Ohlrogge J, Browse J. 1995. Lipid biosynthesis. *Plant Cell* **7**:957–970. doi:10.1105/tpc.7.7.957

1281 Peddie CJ, Collinson LM. 2014. Exploring the third dimension: Volume electron microscopy
1282 comes of age. *Micron* **61**:9–19. doi:10.1016/j.micron.2014.01.009

1283 Pinali C, Kitmitto A. 2014. Serial block face scanning electron microscopy for the study of
1284 cardiac muscle ultrastructure at nanoscale resolutions. *Curr Ther Res - Clin Exp* **76**:1–
1285 11. doi:10.1016/j.yjmcc.2014.08.010

1286 Pinheiro J, Bates M. 2000. Pinheiro - Mixed Effects Models in S & S PLUS. *Springer B*.
1287 doi:org/10.1007/b98882

1288 Plöscher M, Reisinger V, Eichacker LA. 2011. Proteomic comparison of etioplast and
1289 chloroplast protein complexes. *J Proteomics* **74**:1256–1265.
1290 doi:10.1016/j.jprot.2011.03.020

1291 Porra RJ, Thompson WA, Kriedemann PE. 1989. Determination of accurate extinction
1292 coefficients and simultaneous equations for assaying chlorophylls a and b extracted with
1293 four different solvents: verification of the concentration of chlorophyll standards by atomic
1294 absorption spectroscopy. *Biochim Biophys Acta - Bioenerg* **975**:384–394.
1295 doi:https://doi.org/10.1016/S0005-2728(89)80347-0

1296 Pyke KA, Leech RM. 1994. A Genetic Analysis of Chloroplast Division and Expansion in
1297 Arabidopsis thaliana. *Plant Physiol* **104**:201–207. doi:10.1104/pp.104.1.201

1298 Reiland S, Grossmann J, Baerenfaller K, Gehrig P, Nunes-nesi A. 2011. Integrated proteome
1299 and metabolite analysis of the de-etiolation process in plastids from rice (Oryza sativa

L .) **11**:1751–1763. doi:10.1002/pmic.201000703

Richardson LGL, Schnell DJ. 2019. Origins, function, and regulation of the TOC–TIC general protein import machinery of plastids. *J Exp Bot* **71**:1226–1238. doi:10.1093/jxb/erz517

Rudowska L, Gieczewska K, Mazur R, Garstka M, Mostowska A. 2012. Chloroplast biogenesis - correlation between structure and function. *Biochim Biophys Acta* **1817**:1380–7. doi:10.1016/j.bbabio.2012.03.013

Runge S, Sperling U, Frick G, Apel K, Armstrong GA. 1996. Distinct roles for light-dependent NADPH:protochlorophyllide oxidoreductases (POR) A and B during greening in higher plants. *Plant J* **9**:513–523. doi:10.1046/j.1365-313X.1996.09040513.x

Scorrano L, De Matteis MA, Emr S, Giordano F, Hajnóczky G, Kornmann B, Lackner LL, Levine TP, Pellegrini L, Reinisch K, Rizzuto R, Simmen T, Stenmark H, Ungermann C, Schuldiner M. 2019. Coming together to define membrane contact sites. *Nat Commun* **10**:1–11. doi:10.1038/s41467-019-09253-3

Solymosi K, Schoefs B. 2010. Etioplast and etio-chloroplast formation under natural conditions: The dark side of chlorophyll biosynthesis in angiosperms. *Photosynth Res* **105**:143–166. doi:10.1007/s11120-010-9568-2

Spicher L, Glauser G, Kessler F. 2016. Lipid Antioxidant and Galactolipid Remodeling under Temperature Stress in Tomato Plants. *Front Plant Sci* **7**:1–12. doi:10.3389/fpls.2016.00167

Tomizioli M, Lazar C, Brugière S, Burger T, Salvi D, Gatto L, Moyet L, Breckels LM, Hesse A-M, Lilley KS, Seigneurin-Berny D, Finazzi G, Rolland N, Ferro M. 2014. Deciphering Thylakoid Sub-compartments using a Mass Spectrometry-based Approach. *Mol Cell Proteomics* **13**:2147–2167. doi:10.1074/mcp.M114.040923

Türker C, Akal F, Joho D, Panse C, Barkow-Oesterreicher S, Rehrauer H, Schlapbach R. 2010. B-Fabric: The Swiss Army Knife for Life SciencesProceedings of the 13th International Conference on Extending Database Technology, EDBT '10. New York, NY, USA: Association for Computing Machinery. pp. 717–720. doi:10.1145/1739041.1739135

Van Bezouwen LS, Caffarri S, Kale R, Kouřil R, Thunnissen AMWH, Oostergetel GT, Boekema EJ. 2017. Subunit and chlorophyll organization of the plant photosystem II supercomplex. *Nat Plants* **3**:1–11. doi:10.1038/nplants.2017.80

1330 Van Wijk KJ, Kessler F. 2017. Plastoglobuli: Plastid Microcompartments with Integrated
1331 Functions in Metabolism, Plastid Developmental Transitions, and Environmental
1332 Adaptation. *Annu Rev Plant Biol* **68**:253–289. doi:10.1146/annurev-arplant-043015-
1333 111737

1334 Von Wettstein D, Gough S, Kannangara CG. 1995. Chlorophyll Biosynthesis. *Plant Cell*
1335 **7**:1039–1057. doi:10.1105/tpc.7.7.1039

1336 Wang BC, Pan YH, Meng DZ, Zhu YX. 2006. Identification and quantitative analysis of
1337 significantly accumulated proteins during the Arabidopsis seedling de-etiolation process.
1338 *J Integr Plant Biol* **48**:104–113. doi:10.1111/j.1744-7909.2006.00215.x

1339 Weier TE, Brown DL. 1970. Formation of the Prolamellar Body in 8-Day, Dark-Grown
1340 Seedlings. *Am J Bot* **57**:267–275. doi:10.2307/2485302

1341 Wietrzynski W, Schaffer M, Tegunov D, Albert S, Kanazawa A, Plitzko JM, Baumeister W,
1342 Engel BD. 2020. Charting the native architecture of chlamydomonas thylakoid
1343 membranes with single-molecule precision. *Elife* **9**:1–18. doi:10.7554/eLife.53740

1344 Yoshida Y. 2018. Insights into the mechanisms of chloroplast division. *Int J Mol Sci* **19**:1–13.
1345 doi:10.3390/ijms19030733

1346

1347

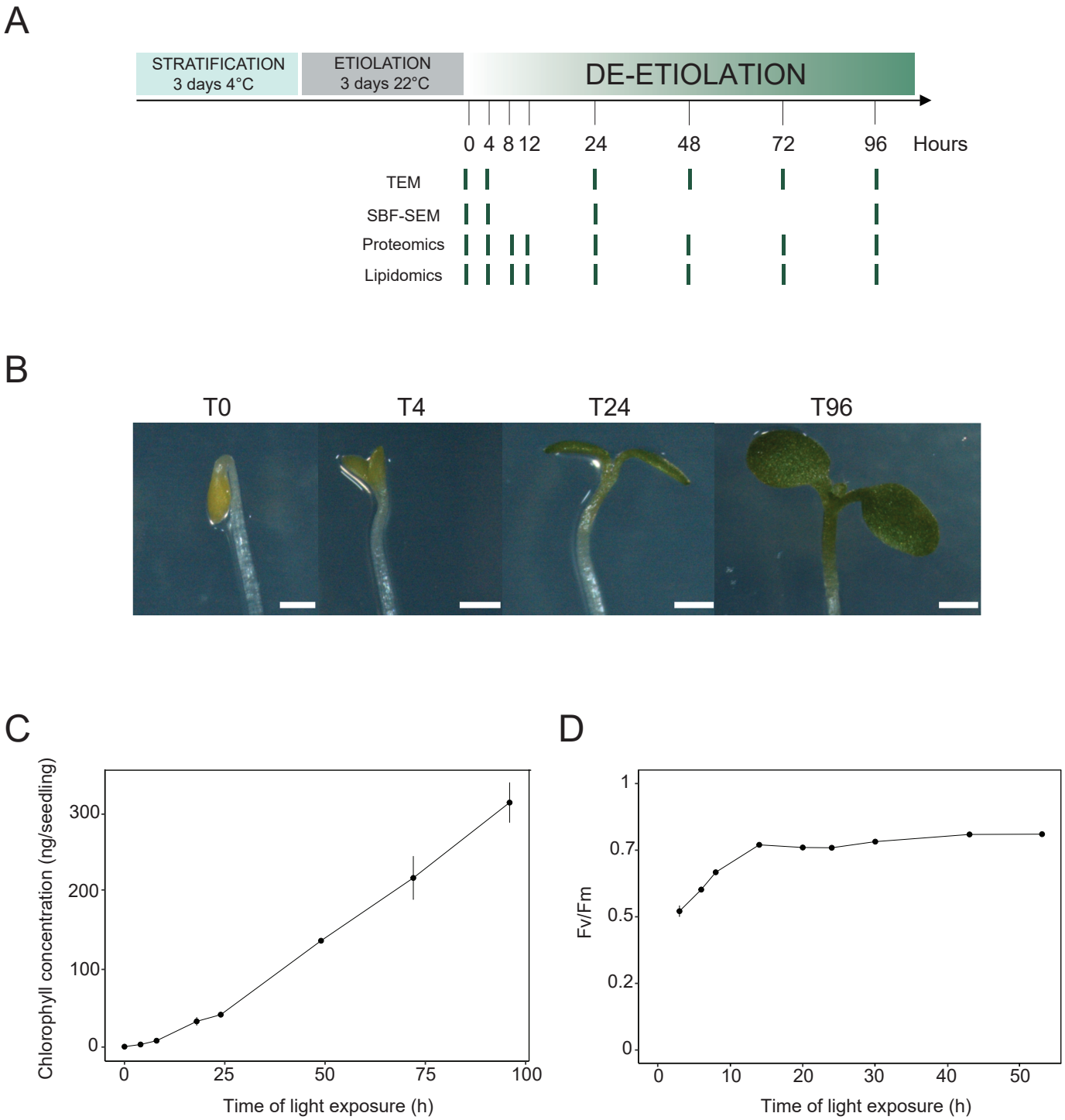

Figure 1: Photosynthesis onset during de-etiolation. (A) Scheme of the experimental design. Seeds of Arabidopsis thaliana (Columbia) sown on agar plates were stratified for three days at 4°C and then transferred to 22°C in the dark. After three days, etiolated seedlings were exposed to continuous white light (40 µmol/m2/s) and harvested at different time points during de-etiolation. Selected time points used for different analyses are indicated. (B) Cotyledon phenotype of etiolated seedlings (T0) after 4 h (T4), 24 h (T24), and 96 (T96) h in continuous white light. Scale bars: 0.5 mm. (C) Chlorophyll quantification at different time points upon illumination. Error bars indicate ± SD (n=3). (D) Maximum quantum yield of photosystem II (Fv/Fm). Error bars indicate ± SD (n=4–10). For some data points, the error bars are inferior to the size of the symbol. Measurements of further photosynthetic parameters are presented in Figure 1- figure supplement 1.

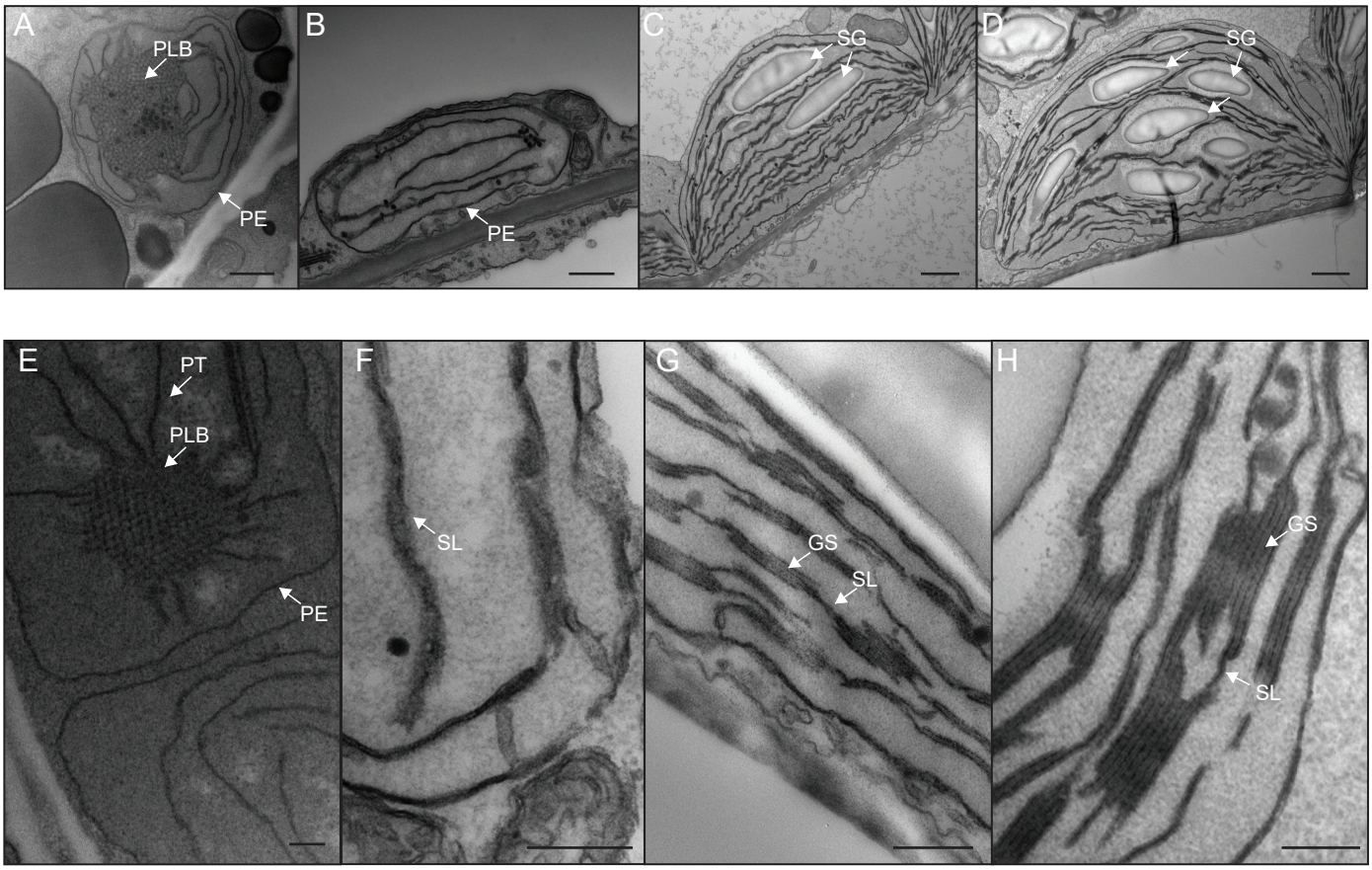

Figure 2: Qualitative analysis of chloroplast ultrastructure during de-etiolation. Transmission electron microscopy (TEM) images of cotyledon cells of 3-day-old, dark-grown Arabidopsis thaliana (Columbia) seedlings illuminated for 0 h (A and E), 4 h (B and F), 24 h (C and G), and 96 h (D and H) in continuous white light (40 µmol/m2/s). (A–D) Scale bars: 500 nm, (E–H) higher magnification of A–D images; Scale bars: 200 nm. PLB: prolamellar body; PT: prothylakoid; PE: plastid envelope; SG: starch grain; GS: grana stack; SL: single lamella. Specific details for measurements of lamella thickness are provided in Figure 2- figure supplement 1.

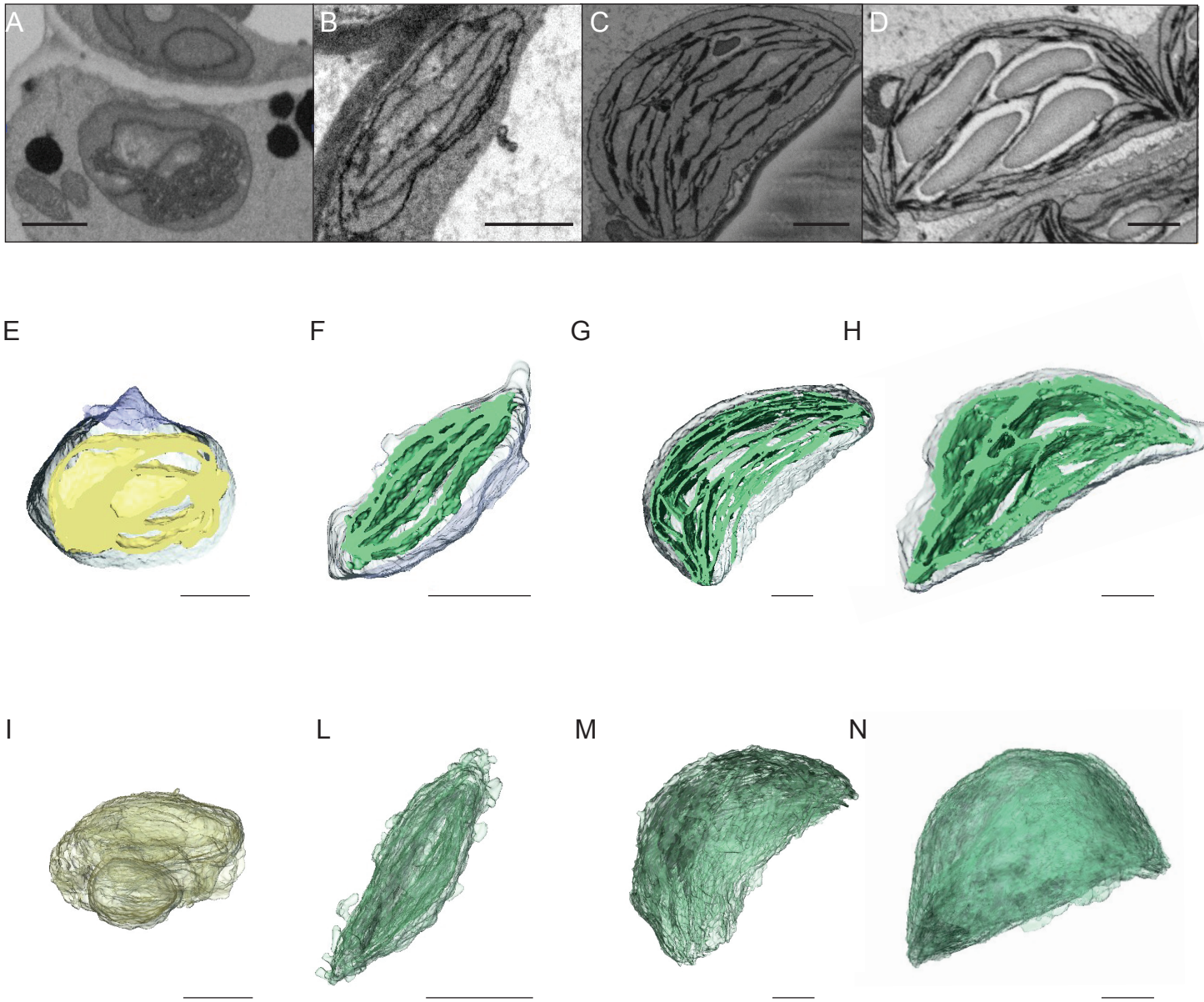

Figure 3: 3D reconstructions of chloroplast thylakoid network during de-etiolation. (A–D) Scanning electron microscopy (SEM) micrographs of representative etioplasts and chloroplasts from 3-day-old, dark-grown Arabidopsis thaliana seedlings illuminated for 0 h (T0; A), 4 h (T4; B), 24 h (T24; C), and 96 h (T96; D) in continuous white light (40 µmol/m2/s). (E–H) Partial 3D reconstruction of thylakoid membranes (green) and envelope (blue) at T0 (E), T4 (F), T24 (G) and T96 (H). Z-depth of thylakoid membrane reconstruction corresponds to 0.06 µm (E), 0.10 µm (F), 0.13 µm (G), and 0.15 µm (H). (I–N). 3D reconstruction of a thylakoid membrane of an etioplast at T0 (I) or a chloroplast at T4 (L), T24 (M), and T96 (N). Scale bars = 1 µm. Details of grana segmentation at T24 are provided in Figure 3- figure supplement 1.

A

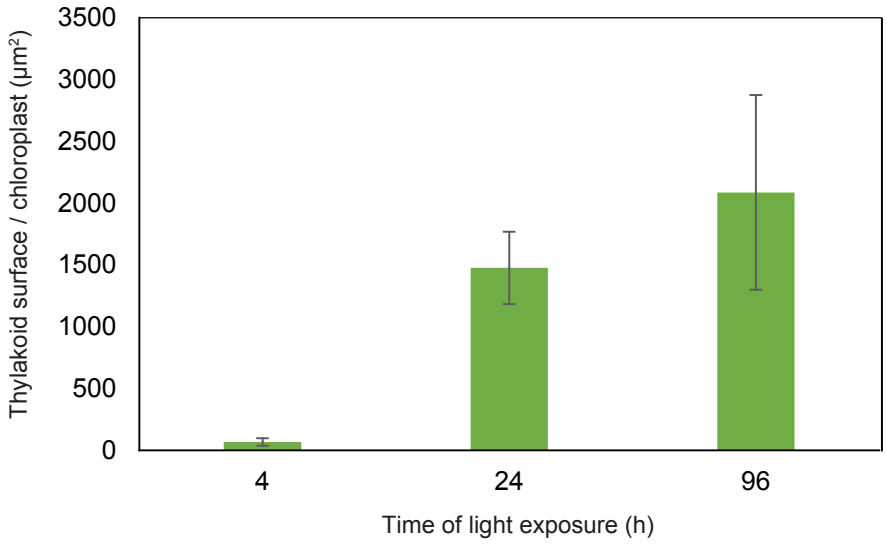

B

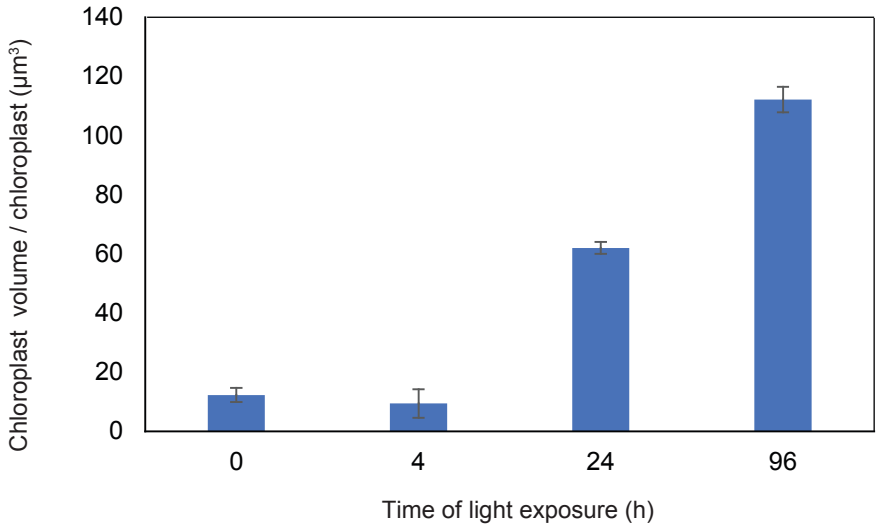

Figure 4: Quantitative analysis of chloroplast volume and thylakoid surface during de-etiolation. Quantification of thylakoid surface per chloroplast (A) and chloroplast volume (B) using 3-day-old, dark-grown Arabidopsis thaliana (Columbia) seedlings illuminated for 0 h, 4 h, 24 h, and 96 h in continuous white light (40 µmol/ m2/s). Morphometric data were quantified by Labels analysis module of Amira software. Error bars indicate ± SD (n=3). The total thylakoid surface indicated in A corresponds to the thylakoid surface exposed to the stroma, calculated in Amira software, in addition to the percentage of the grana surface (%Gs) calculated as described in Figure 3- figure supplement 1.

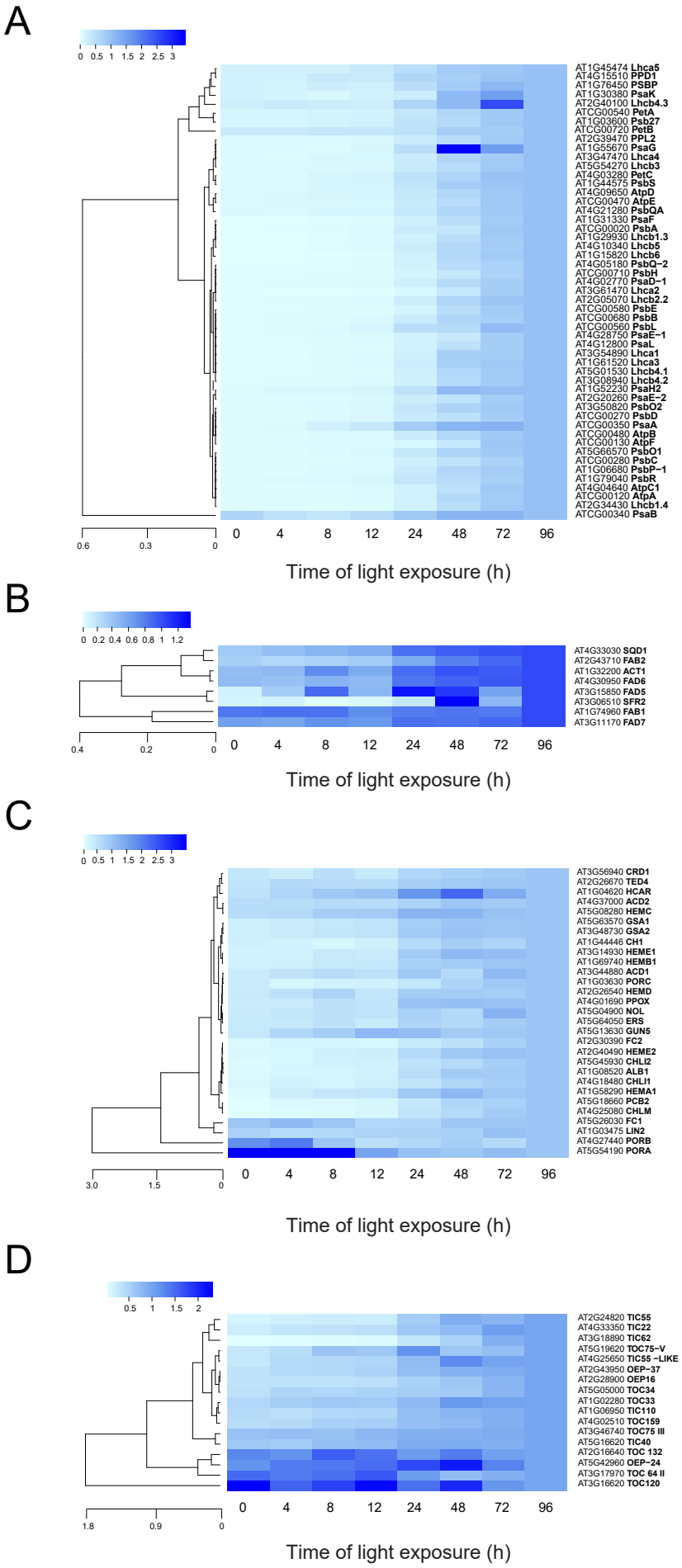

Figure 4: Quantitative analysis of chloroplast volume and thylakoid surface during de-etiolation. Quantification of thylakoid surface per chloroplast (A) and chloroplast volume (B) using 3-day-old, dark-grown Arabidopsis thaliana (Columbia) seedlings illuminated for 0 h, 4 h, 24 h, and 96 h in continuous white light (40 µmol/m2/s). Morphometric data were quantified by Labels analysis module of Amira software. Error bars indicate ± SD (n=3). The total thylakoid surface indicated in A corresponds to the thylakoid surface exposed to the stroma, calculated in Amira software, in addition to the percentage of the grana surface (%Gs) calculated as described in Figure 3- figure supplement 1.

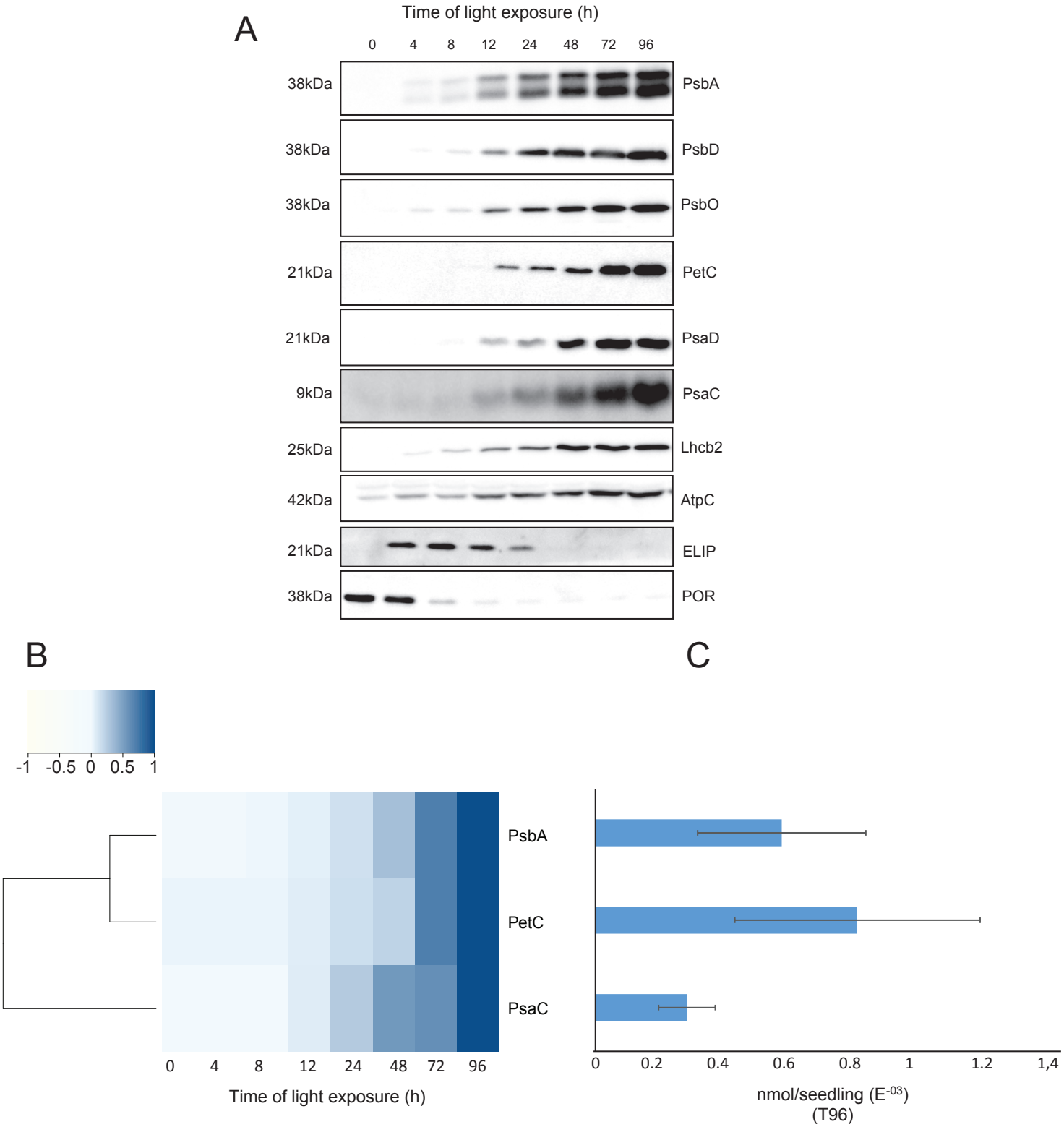

Figure 6: Accumulation dynamics of photosynthesis-related proteins during de-etiolation. 3-day-old etiolated seedlings of *Arabidopsis thaliana* were illuminated for 0 h (T0), 4 h (T4), 8 h (T8), 12 h (T12), 24 h (T24), 48 h (T48), 72 h (T72), and 96 h (T96) under white light (40 µmol/m2/s). (A) Proteins were separated by SDS-PAGE and transferred onto nitrocellulose membrane and immunodetected with antibodies against PsbA, PsbD, PsbO, PetC, PsaD, PsaC, Lhcb2, AtpC, ELIP, POR proteins. (B–C) Quantification of PsbA, PetC, and PsaC during de-etiolation. Heatmap (B) was generated after normalization of the amount of each protein relative to the last time point (T96). Graph (C) corresponds to the absolute quantification of proteins at T96. Error bars indicate ± SD (n=3). Quantification of photosystem-related proteins during de-etiolation is detailed in Figure 6- figure supplement 1.

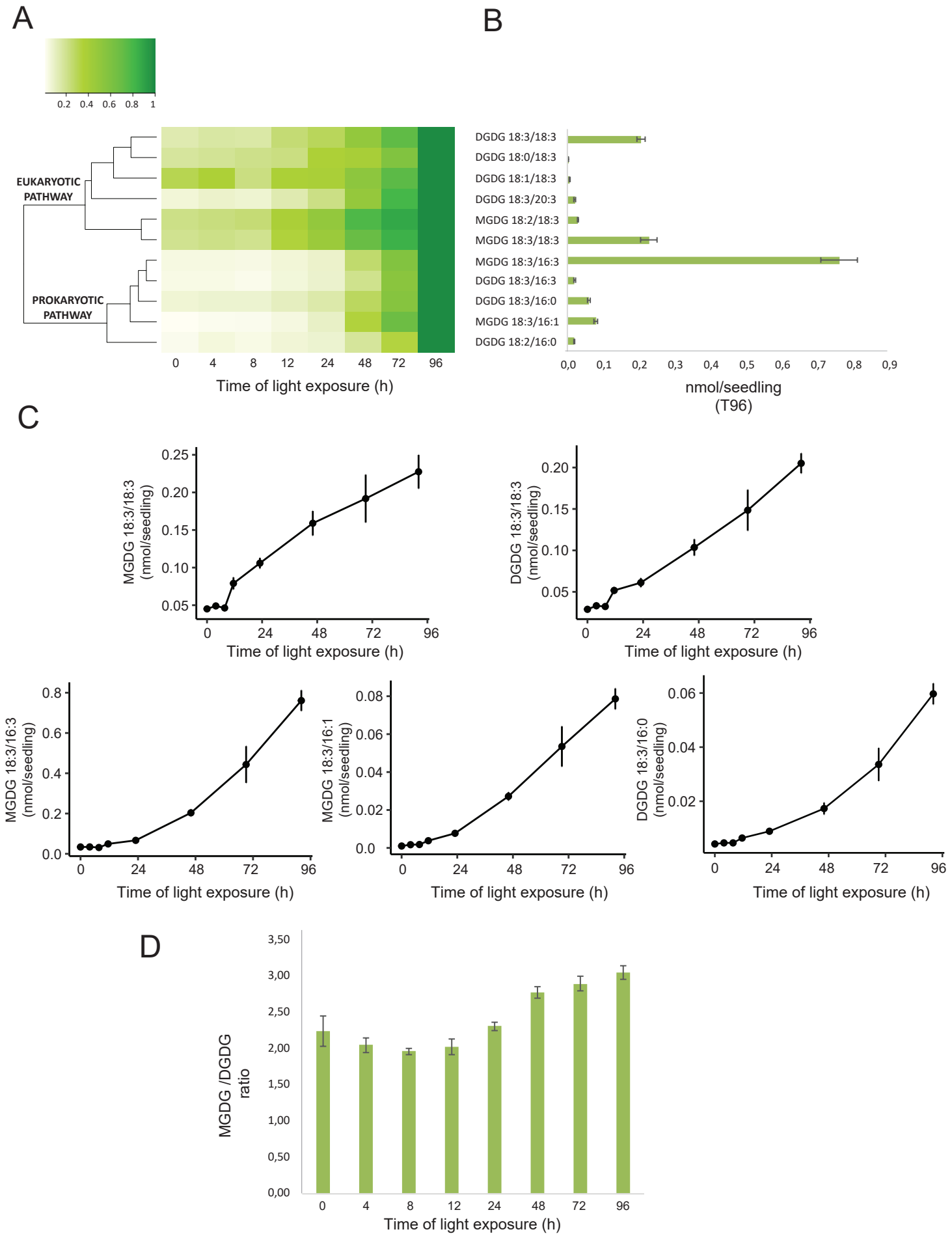

Figure 7: Accumulation dynamics of galactolipids during de-etiolation. 3-day-old etiolated seedlings of *Arabidopsis thaliana* were illuminated for 0 h (T0), 4 h (T4), 8 h (T8), 12 h (T12), 24 h (T24), 48 h (T48), 72 h (T72), and 96 h (T96) under white light (40 µmol/m2/s). (A) Heatmap representation of galactolipids (MGDG and DGDG) during de-etiolation. Samples were normalized to the last time point (T96). (B) Absolute quantification at T96 expressed in nmol/seedling. Error bars indicate ± SD (n=4). (C) Absolute quantification (nmol/seedling) of the most abundant chloroplast galactolipids MGDG (MGDG 18:3/18:3, MGDG 18:3/16:3, MGDG 18:3/16:1) and DGDG (DGDG 18:3/18:3, DGDG 18:3/16:0) at different time points during de-etiolation. Error bars indicate ± SD (n=4). (D) The MGDG/DGDG ratio was calculated using all 12 species of galactolipids detected during de-etiolation. Error bars indicate ± SD (n=4).

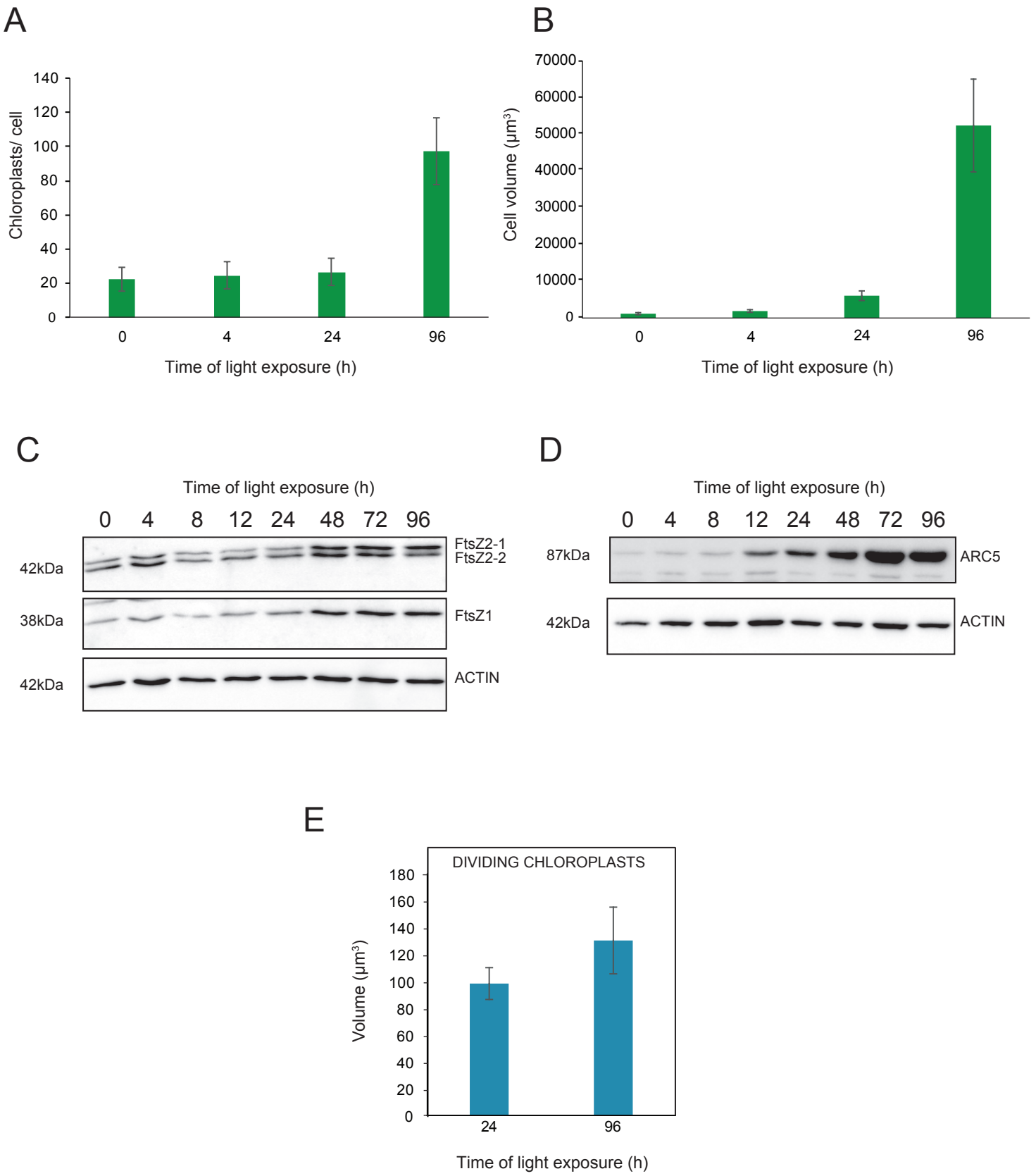

Figure 8: Relationship between chloroplast proliferation and chloroplast volume. (A-B) Chloroplast number and cell volume in cotyledons of 3-day-old, dark-grown Arabidopsis thaliana seedlings illuminated for 0 h (T0), 4 h (T4), 24 h (T24), and 96 h (T96) in continuous white light (40 µmol/m2/s). (A) Chloroplast number per cell during de-etiolation. Error bars indicate ± SD (n=6 for T0 and T7; 7 for T24; 5 for T96). (B) Cell volume was quantified by the Labels analysis module of Amira software. Error bars indicate ± SD (n=5–6). (C–D) Total proteins were extracted from T0–T96 seedlings, separated on SDS-PAGE, and transferred onto nitrocellulose. Proteins involved in plastid division (C, FtsZ; D, ARC5) and loading control (actin) were detected using specific antibodies (FtsZ2 antibody recognizes both FtsZ2-1 and FtsZ2-2). (E) Volume of dividing chloroplast at T24 and T96. Error bars indicate ± SD (n=3). Further details of chloroplast proliferation in parallel with cell expansion are provided in Figure 8- figure supplement 1.

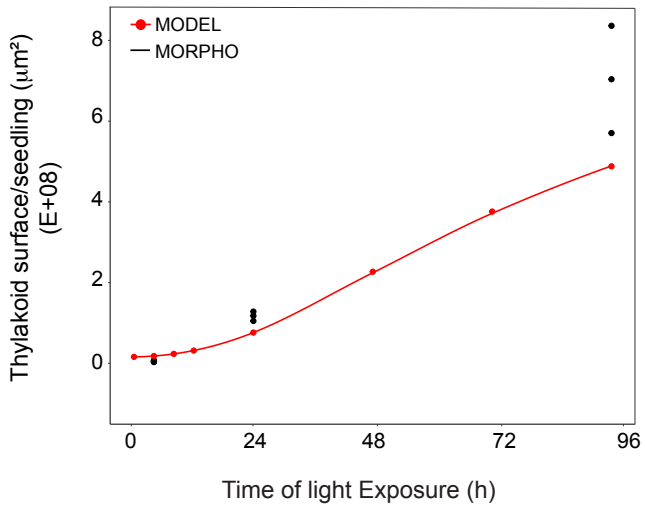

Figure 9: Superimposition of thylakoid surface per seedling obtained from morphometric analysis and mathematical modeling. Thylakoid surface per seedling was estimated using quantitative data from 3View analysis ('MORPHO' black dots at T4, T24, and T96; and see Figure 4 and Table 1) and model generated using the quantitative data from proteomics and lipidomics ('MODEL' red line at T0, T4, T8, T12, T24, T48, T72, and T96, and Table 1). Further details are provided in Figure 9- figure supplement 1 and 2.

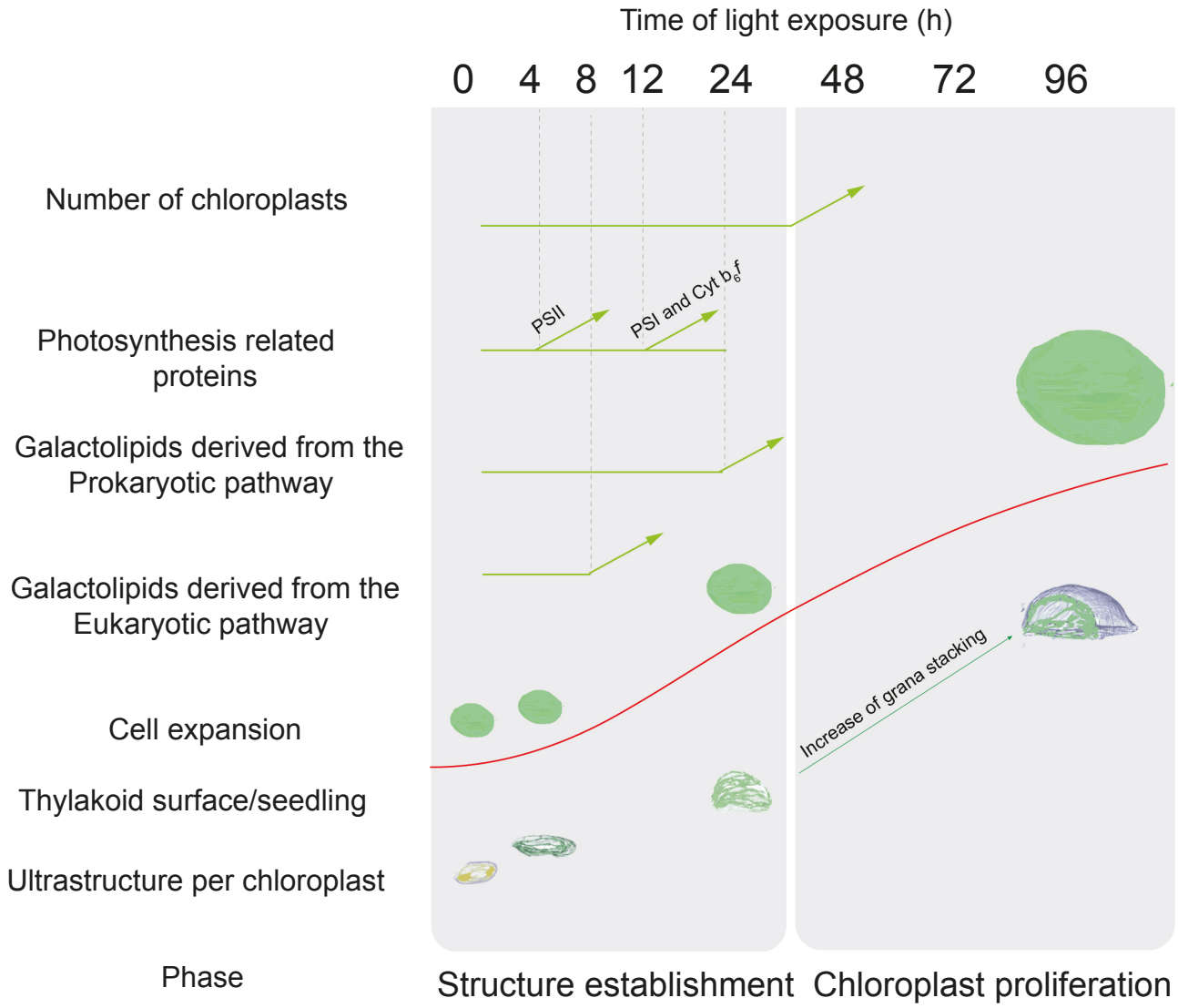

Figure 10: Overview of changes observed during the de-etiolation process in Arabidopsis thaliana seedlings. The 'Structure Establishment Phase' is correlated with disassembly of the PLB and gradual formation of the thylakoid membrane as well as an initial increase of eukaryotic (after 8 h) and prokaryotic (after 24 h) galactolipids and photosynthesis-related proteins (PSII subunits at 4 h, PSI and cyt b6f at 12 h). The subsequent 'Chloroplast Proliferation Phase' is associated with an increase in chloroplast number in concomitance with cell expansion, a linear increase of prokaryotic and eukaryotic galactolipids and photosynthesis-related proteins, and increased grana stacking. The red curve (retrieved from the Figure 9) shows thylakoid surface/seedling dynamics during the de-etiolation process.